PHYSICAL REVIEW D **90,** 115002 (2014)

Model-independent probe of anomalous heavy neutral Higgs bosons at the LHC

Yu-Ping Kuang,[1,2,*] Hong-Yu Ren,[1,†] and Ling-Hao Xia[1,‡]

[1]*Department of Physics, Tsinghua University, Beijing 100084, China*
[2]*Center for High Energy Physics, Tsinghua University, Beijing 100084, China*

(Received 24 April 2014; published 3 December 2014)

We first formulate, in the framework of the effective Lagrangian, the general form of the effective interactions of the lightest Higgs boson h and a heavier neutral Higgs boson H in a multi-Higgs system taking account of the Higgs mixing effect. We regard h as the discovered Higgs boson which has been shown to be consistent with the standard model Higgs boson. The obtained effective interactions contain extra parameters reflecting the Higgs mixing effect. Next, we study the constraints on the anomalous coupling constants of H from both the requirement of the unitarity of the S matrix and the exclusion bounds on the standard model Higgs boson obtained from the experimental data at the 7–8 TeV LHC. From this we obtain the available range of the anomalous coupling constants of H, with which H is not excluded by the yet known theoretical and experimental constraints. We then study the signatures of H at the 14 TeV LHC. In this paper, we suggest taking weak-boson scattering and $pp \to VH^* \to VVV$ as sensitive processes for probing H model independently at the 14 TeV LHC. We take several examples with the anomalous HVV coupling constants in the available ranges to do the numerical study. A full tree-level calculation at the hadron level is given with signals and backgrounds carefully calculated. We impose a series of proper kinematic cuts to effectively suppress the backgrounds. It is shown that, in both the VV scattering and the $pp \to VH^* \to VVV$ processes, the H boson can be discovered from the invariant mass distributions of the final state particles with reasonable integrated luminosity. Especially, in the $pp \to VH^* \to VVV$ process, the invariant mass distribution of the final state jets can show a clear resonance peak of H. Finally, we propose several physical observables from which the values of the anomalous coupling constants f_W and f_{WW} can be measured experimentally.

DOI: 10.1103/PhysRevD.90.115002 PACS numbers: 14.80.Ec, 12.60.Fr, 12.15.-y

I. INTRODUCTION

The discovery of the 125–126 GeV Higgs boson [1] at the LHC in 2012 is a milestone in our understanding of electroweak (EW) theory. So far, the measured gauge and Yukawa couplings of this 125–126 GeV Higgs boson are consistent with the standard model (SM) couplings [2]. Since the precision of the present measurements at the LHC is still rather mild due to the large hadronic backgrounds, a new high energy electron-positron collider is expected for higher precision measurements of the Higgs properties [3]. However, even if the measured precise values of the 125–126 GeV Higgs boson couplings are very close to the SM values, it does not imply that the SM is a final theory of fundamental interactions since the SM suffers from various shortcomings, such as the well-known theoretical problems of *triviality* [4] and *unnaturalness* [5], the fact that it does not include the dark matter, that it can neither predict the mass of the Higgs boson nor predict the masses of all the fermions, etc. Searching for new physics beyond the SM is the most important goal of future particle physics studies.

Most new physics models contain more than one Higgs boson. In many well-known new physics models [such as the two-Higgs-doublet models, the minimal supersymmetric extension of the SM, the left-right symmetric models, etc.], the lightest Higgs boson may behave rather like a SM Higgs boson, and the masses of other heavy Higgs bosons are usually in the few hundred GeV to TeV range. So it is quite possible that the discovered 125–126 GeV Higgs is the lightest Higgs boson in certain new physics models. Since the few hundred GeV to TeV range is within the searching ability of the LHC, searching for nonstandard (NS) heavy neutral Higgs bosons at the 14 TeV LHC is thus a feasible way of finding out the correct new physics model beyond the SM.

There are a lot of proposed new physics models in the literatures in which the Higgs bosons can be either elementary or composite, and we actually do not know whether the correct new physics model reflecting the nature is just one of these proposed models or not. Therefore, just searching for heavy Higgs bosons model by model at the LHC is not an effective way. For example, there have been experimental searches for the heavy Higgs bosons in the minimal supersymmetric extension of the SM and the two-Higgs-doublet models with negative results [6–8]. A more

*ypkuang@mail.tsinghua.edu.cn
†renhy10@mails.tsinghua.edu.cn
‡xlh10@mails.tsinghua.edu.cn

effective way is to perform a general search for the heavy neutral Higgs boson model independently.

In the following, we shall treat the discovered 125–126 GeV Higgs boson as a SM-like Higgs with negligible anomalous couplings [9]. For a neutral heavier Higgs boson with not so small gauge interactions (there may be gauge-phobic heavy neutral Higgs bosons which are not considered in the present study), we shall give a general model-independent formulation of the gauge and Yukawa couplings of the NS heavy neutral Higgs boson in a multi-Higgs system taking account of the Higgs mixing effect based on the effective Lagrangian consideration, which contains several unknown coupling constants. We then study the constraints on the unknown coupling constants both theoretically and experimentally. We shall first study the theoretical upper bounds on these unknown coupling constants from the requirement of the unitarity of the S matrix. Then we shall consider the 95% C.L. experimental exclusion limits on the SM Higgs boson obtained from the CMS (ATLAS) data at the 7–8 TeV LHC [10–14]. The condition for the NS heavy neutral Higgs bosons to avoid being excluded is that they should have large enough anomalous couplings to sufficiently reduce their production rates. These bounds provide certain knowledge on the possible range of these unknown coupling constants, which can be a starting point of our study of the model-independent detection of the NS heavy neutral Higgs boson H at the LHC.

In this paper, we consider a general multi-Higgs system with Higgs mixing caused by the general multi-Higgs interactions. In the mass eigenstate, we pay special attention to the lightest Higgs boson h and the heavier Higgs boson (heavier than h but lighter than other heavy Higgs bosons) H. We regard h as the discovered 125–126 GeV Higgs boson which has been shown to be consistent with the SM Higgs boson. We then formulate the effective interactions related to h and H up to the dim-6 operators. Since h is consistent with the SM Higgs boson, we neglect its dim-6 interactions. The obtained effective interactions are different from the conventional one constructed for a single-Higgs system [15] by containing extra new parameters reflecting the Higgs mixing effect.

Next, we study the existing theoretical and experimental constraints on the parameters in the effective interactions. Theoretically, we require that the present theory does not violate the unitarity of the S matrix. Experimentally, we require that the heavy Higgs boson H is not excluded by the CMS (ATLAS) exclusion bound on the SM Higgs boson [10]. These constraints determine an *available* region for the anomalous coupling constants with which the heavy Higgs boson H is not excluded by the present theoretical and experimental requirements. This provides the staring point of studying the model-independent probe of the heavy Higgs boson H at the 14 TeV LHC.

In this paper, we suggest taking weak-boson scattering and $pp \to VH^* \to VVV$ $(V = W, Z)$ as two sensitive processes to probe H at the LHC. To have large enough cross sections, we take the semileptonic mode in the final states. We shall carefully analyze the signal, irreducible background (IB), and all possible reducible backgrounds (RBs), and impose a series of kinematic cuts to effectively suppress the backgrounds. We shall see that the heavy Higgs boson H can be detected with reasonable integrated luminosities at the 14 TeV LHC. Especially in the $pp \to VH^* \to VVV$ process, a clear resonance peak of H can be seen experimentally.

Finally, we propose several physical observables from which the anomalous coupling constants f_W and f_{WW} can be measured experimentally. This provides a new high energy criterion for new physics models beyond the SM. Only new physics models giving f_W and f_{WW} consistently with the measured values can survive, otherwise the models will be ruled out by this new criterion. This helps us to find out the correct new physics model reflecting the nature step by step.

This paper is organized as follows. Sections II–IV are on studying the formulation of the effective interactions and their constraints. Sections V–VIII are on the study of the LHC signatures of H. In Sec. II we present the details of the formulation of the model-independent gauge and Yukawa couplings of H in which the anomalous gauge couplings are up to the dim-6 operators. Section III is the study of the theoretical constraints on the unknown coupling constants from the requirement of the unitarity of the S matrix. In Sec. IV, we study how the CMS 95% exclusion limit on the SM Higgs boson leads to the lower bounds on the unknown coupling constant. Combining the constraints given in Secs. III and IV, we get the *available* range of the anomalous coupling constants, with which H is not excluded by the yet known theoretical and experimental constraints. Section V is a brief description of the general features of studying the LHC signatures of H. In Sec. VI, we shall study the signal, IB, and all the possible RBs in weak-boson scattering, and we take proper kinematic cuts for effectively suppressing the backgrounds from analyzing the properties of the signal and backgrounds. Then we show how the $M_H = 400$, 500, and 800 GeV heavy neutral Higgs boson can be detected at the 14 TeV LHC. Section VII is the study of the $pp \to VH^* \to VVV$ process. We shall show that this process is more sensitive than weak-boson scattering in the sense that the resonance peak can be clearly seen, and the required integrated luminosity is lower. In Sec. VIII, we shall show that the anomalous coupling constants f_W and f_{WW} can be measured by measuring both the cross section and certain observable distributions of the final state particles. Section IX is a concluding remark.

II. ANOMALOUS COUPLINGS OF THE NONSTANDARD HEAVY NEUTRAL HIGGS BOSONS

For generality, we shall not specify the EW gauge group of the new physics theories under consideration. The only

requirement is that the gauge group should contain an $SU(2)_L \times U(1)$ subgroup with the gauge fields W, Z, and γ. Also, we shall not specify the number of Higgs bosons and their group representations, so that a Higgs boson in the Lagrangian may be $SU(2)_L$ singlets, doublets, etc.

Let $\Phi_1, \Phi_2, \cdots\cdots$ be the original Higgs fields [in various $SU(2)_L$ representations] in the Lagrangian. The multi-Higgs potential $V(\Phi_1, \Phi_2, \cdots\cdots)$ will, in general, cause mixing between $\Phi_1, \Phi_2, \cdots\cdots$ to form the mass eigenstates. Let Φ_h and Φ_H be the lightest Higgs and a heavier neutral heavy Higgs fields with Higgs bosons h and H (the neutral Higgs boson is just heavier than h and lighter than other heavy Higgs bosons), respectively (gauge-phobic neutral heavy Higgs bosons are not considered in this study). They are, in general, mixtures of $\Phi_1, \Phi_2, \cdots\cdots$. So their vacuum expectation values (VEVs) v_h, v_H are not the same as the SM VEV $v = 246$ GeV.

In the following, we shall consider the anomalous Yukawa couplings and anomalous gauge couplings separately.

A. Anomalous Yukawa couplings

The anomalous Yukawa couplings are relevant to our study of Higgs decays. We are not interested in multi-Higgs-fermion couplings which are irrelevant to our study.

As we have mentioned, we treat the 125–126 GeV Higgs boson h as SM-like, i.e., with negligible anomalous couplings. So that the Yukawa couplings of Φ_h to a fermion f is

$$y_f^h \bar{\psi}_f \Phi_h \psi_f, \tag{1}$$

where y_f^h is the Φ_h-f-$\bar{f}$ Yukawa coupling constant which is close to the SM Yukawa coupling constant $y_f^{\rm SM}$.

For a NS heavy neutral Higgs boson Φ_h, its Yukawa coupling may not be the same as the standard Yukawa coupling. It can be seen that up to dim-6 operators, there is no new coupling form other than the dim-4 Yukawa coupling contributing [16]. We thus formulate the anomalous Yukawa coupling of Φ_H to a fermion f by

$$y_f^H \bar{\psi}_f \Phi_H \psi_f \equiv C_f y_f^{\rm SM} \bar{\psi}_f \Phi_H \psi_f, \tag{2}$$

where C_f is the anomalous factor of the Yukawa coupling. When $C_f = 1$, the coupling y_f^H equals to the SM coupling y_f. In our study, the mostly relevant fermion is the t quark since C_t concerns the H-g-g vertex, i.e., the Higgs production rate and the $H \to gg$ (Higgs decays to light hadrons) rate, and the $H \to t\bar{t}$ decay rate as well.

The value of C_t depends on the mixing between different neutral Higgs bosons. So far there is no clear experimental constraint on C_t. In the proposed new physics models, some of the NS heavy neutral Higgs bosons have $C_t \approx 1$, while some of the NS heavy neutral Higgs bosons have $C_t < 1$.

In our following studies, we consider both possibilities. We regard the $C_t \approx 1$ case as type I, and the $C_t < 1$ case as type II.

Note that there are more than one Higgs bosons contributing to the fermion mass m_f, i.e.,

$$m_f = \frac{1}{\sqrt{2}}\{y_f^h v_h + y_f^H v_H + \cdots\cdots\}. \tag{3}$$

We know that, with the SM Yukawa coupling $y_f^{\rm SM}$ and $v = 246$ GeV, $m_f = y_f^{\rm SM} v/\sqrt{2}$. Comparing this with (3), we obtain

$$\left\{\frac{y_f^h}{y_f^{\rm SM}}\frac{v_h}{v} + \frac{y_f^H}{y_f^{\rm SM}}\frac{v_H}{v} + \cdots\cdots\right\} = 1. \tag{4}$$

This serves as a constraint on the Yukawa coupling constants and VEVs.

B. Anomalous gauge couplings

The effective gauge couplings of a Higgs boson in the multi-Higgs system taking account of the Higgs mixing effect have not been given in the published papers. We formulate them in the following.

We first consider the lightest Higgs boson h. Because of Higgs mixing, the gauge coupling constant g_h of the lightest Higgs field Φ_h may not be the same as the $SU(2)_L$ gauge coupling constant g. For a SM-like lightest Higgs boson, g_h is close to g. With negligible anomalous couplings, the dim-4 gauge couplings of the lightest Higgs field is

$$\begin{aligned}
\mathcal{L}^{(4)}_{hWW} &= \frac{1}{2} g_h^2 v_h h W_\mu W^\mu \approx g M_W \rho_h h W_\mu W^\mu, \\
\mathcal{L}^{(4)}_{hZZ} &= \frac{1}{4c^2} g_h^2 v_h h Z_\mu Z^\mu \approx \frac{g M_W \rho_h}{2c^2} h Z_\mu Z^\mu, \\
\rho_h &\equiv \frac{g_h^2 v_h}{g^2 v},
\end{aligned} \tag{5}$$

where g is the $SU(2)_L$ gauge coupling, $v = 246$ GeV, M_W is the W boson mass, and $c \equiv \cos\theta_W$.

For the NS heavy neutral Higgs boson H, its gauge coupling g_H may not be close to g due to the Higgs mixing depending on the property of H. Similar to (5), the dim-4 gauge coupling of H is

$$\begin{aligned}
\mathcal{L}^{(4)}_{HWW} &= \frac{1}{2} g_H^2 v_H H W_\mu W^\mu \approx g M_W \rho_H H W_\mu W^\mu, \\
\mathcal{L}^{(4)}_{HZZ} &= \frac{1}{4c^2} g_H^2 v_H H Z_\mu Z^\mu \approx \frac{g M_W \rho_H}{2c^2} H Z_\mu Z^\mu, \\
\rho_H &\equiv \frac{g_H^2 v_H}{g^2 v};
\end{aligned} \tag{6}$$

Eq. (6) differs from the SM form only by an extra factor ρ_H, i.e., $g^2 v \Rightarrow g^2 v \rho_H$. Since ρ_H depends on the specific mixing between H and other Higgs bosons, we take it as an unknown parameter here.

Beyond the dim-4 coupling (6), there can also be dim-6 anomalous gauge couplings of H. The form of the dim-6 anomalous gauge couplings for a single-Higgs system (with the dim-4 coupling the same as the SM interaction) was given in Refs. [15,18] and a detailed review of this was given in Ref. [19]. Now we are dealing with a multi-Higgs system with the dim-4 coupling shown in Eq. (6). Referring to the relation between the dim-4 and dim-6 couplings given in Refs. [15,19], we write down our dim-6 couplings as

$$\mathcal{L}^{(6)}_{HVV} = \sum_n \frac{f_n}{\Lambda^2}\mathcal{O}_n, \tag{7}$$

where Λ is the scale below which the effective Lagrangian holds. When it is needed to specify the value of Λ in some cases, we shall take $\Lambda = 3$ TeV as an example. The gauge-invariant dimension-6 operators $\mathcal{O}_n$'s are

$$\begin{aligned}
&\mathcal{O}_{BW} = \Phi_H^\dagger \hat{B}_{\mu\nu}\hat{W}^{\mu\nu}\Phi_H, \quad \mathcal{O}_{DW} = \mathrm{Tr}([D_\mu, \hat{W}_{\nu\rho}],[D^\mu, \hat{W}^{\nu\rho}]),\\
&\mathcal{O}_{DB} = -\frac{g'^2}{2}(\partial_\mu B_{\nu\rho})(\partial^\mu B^{\nu\rho}),\\
&\mathcal{O}_{\Phi,1} = (D_\mu \Phi_H)^\dagger \Phi_H^\dagger \Phi_H (D^\mu \Phi_H),\\
&\mathcal{O}_{\Phi,2} = \frac{1}{2}\partial^\mu(\Phi_H^\dagger\Phi_H)\partial_\mu(\Phi_H^\dagger\Phi_H), \quad \mathcal{O}_{\Phi,3} = \frac{1}{3}(\Phi_H^\dagger\Phi_H)^3,\\
&\mathcal{O}_{WWW} = \mathrm{Tr}[\hat{W}_{\mu\nu}\hat{W}^{\nu\rho}\hat{W}^{\mu}_{\rho}], \quad \mathcal{O}_{WW} = \Phi_H^\dagger \hat{W}_{\mu\nu}\hat{W}^{\mu\nu}\Phi_H,\\
&\mathcal{O}_{BB} = \Phi_H^\dagger \hat{B}_{\mu\nu}\hat{B}^{\mu\nu}\Phi_H,\\
&\mathcal{O}_{W} = (D_\mu\Phi_H)^\dagger \hat{W}^{\mu\nu}(D_\nu\Phi_H),\\
&\mathcal{O}_{B} = (D_\mu\Phi_H)^\dagger \hat{B}^{\mu\nu}(D_\nu\Phi_H),
\end{aligned} \tag{8}$$

where $\hat{B}_{\mu\nu}$ and $\hat{W}_{\mu\nu}$ stand for

$$\hat{B}_{\mu\nu} = i\frac{g'_H}{2}B_{\mu\nu}, \qquad \hat{W}_{\mu\nu} = i\frac{g_H}{2}\sigma^a W^a_{\mu\nu}, \tag{9}$$

in which g_H and g'_H are the $SU(2)_L$ and $U(1)$ gauge coupling constants of H, respectively. It has been shown that the operators $\mathcal{O}_{\Phi,1}, \mathcal{O}_{BW}, \mathcal{O}_{DW}, \mathcal{O}_{DB}$ are related to the two-point functions of the weak bosons, so that they are severely constrained by the precision EW data [19]. For example, $\mathcal{O}_{BW}$ and $\mathcal{O}_{\Phi,1}$ are related to the oblique correction parameters S and T, and are thus strongly constrained by the precision EW data. The 2σ constraints on $|f_{BW}/\Lambda^2|$ and $|f_{\Phi,1}/\Lambda^2|$ are $|f_{BW}/\Lambda^2|, |f_{\Phi,1}/\Lambda^2| < O(10^{-2})$ TeV^{-2} [20]. The operators $\mathcal{O}_{\Phi,2}$ and $\mathcal{O}_{\Phi,3}$ are related to the triple and quartic Higgs boson self-interactions, and have been studied in detail in Ref. [21]. The operator O_{WWW} is related to the weak-boson self-couplings, so that it is irrelevant to the present study. Furthermore, the ATLAS and CMS experiments on testing the triple gauge couplings [22] show stronger and stronger constraints on the anomalous triple gauge coupling. So we ignore the operator $f_{WWW}\mathcal{O}_{WWW}/\Lambda^2$ in our present study. The precision and low energy EW data are not sensitive to the remaining four operators $\mathcal{O}_{WW}, \mathcal{O}_{BB}, \mathcal{O}_W$, and $\mathcal{O}_B$; so these four operators are what we shall pay special attention in our study in high energy processes.

The relevant effective Lagrangian expressed in terms of the photon field A_μ, the weak-boson fields $W^\pm_\mu$, Z_μ, and the Higgs boson field H is

$$\begin{aligned}
\mathcal{L}^{(6)}_{HVV} = {} & g_{H\gamma\gamma}HA_{\mu\nu}A^{\mu\nu} + g^{(1)}_{HZ\gamma}A_{\mu\nu}Z^\mu\partial^\nu H + g^{(2)}_{HZ\gamma}HA_{\mu\nu}Z^{\mu\nu}\\
& + g^{(1)}_{HZZ}Z_{\mu\nu}Z^\mu\partial^\nu H + g^{(2)}_{HZZ}HZ_{\mu\nu}Z^{\mu\nu}\\
& + g^{(1)}_{HWW}(W^+_{\mu\nu}W^{-\mu}\partial^\nu H + \mathrm{H.c.}) + g^{(2)}_{HWW}HW^+_{\mu\nu}W^{-\mu\nu},
\end{aligned} \tag{10}$$

and the anomalous couplings $g^{(i)}_{HVV}$ with $i = 1, 2$ in our case are related to the anomalous couplings f_n's by

$$\begin{aligned}
g_{H\gamma\gamma} &= -gM_W\rho_H\frac{s^2(f_{BB}+f_{WW})}{2\Lambda^2},\\
g^{(1)}_{HZ\gamma} &= gM_W\rho_H\frac{s(f_W - f_B)}{2c\Lambda^2},\\
g^{(2)}_{HZ\gamma} &= gM_W\rho_H\frac{s[s^2 f_{BB} - c^2 f_{WW}]}{c\Lambda^2},\\
g^{(1)}_{HZZ} &= gM_W\rho_H\frac{c^2 f_W + s^2 f_B}{2c^2\Lambda^2},\\
g^{(2)}_{HZZ} &= -gM_W\rho_H\frac{s^4 f_{BB} + c^4 f_{WW}}{2c^2\Lambda^2},\\
g^{(1)}_{HWW} &= gM_W\rho_H\frac{f_W}{2\Lambda^2}, \qquad g^{(2)}_{HWW} = -gM_W\rho_H\frac{f_{WW}}{\Lambda^2},
\end{aligned} \tag{11}$$

in which $s \equiv \sin\theta_W$, $c \equiv \cos\theta_W$. These formulas are similar to those given in Ref. [19] but with an extra factor ρ_H reflecting the Higgs mixing effect in the overall constant.

So including the dim-4 and dim-6 anomalous couplings, there are altogether five new parameters, namely, ρ_H, f_W, f_{WW}, f_B, and f_{BB}. We see from Eq. (11) that the parameters f_B and f_{BB} are not related to the HWW couplings. They appear in the HZZ couplings with the small factors s^2 and s^4, respectively. They mainly contribute to the $H\gamma\gamma$ and $HZ\gamma$ couplings.

The HVV operators in (10) contain extra derivatives relative to (6). So that $\mathcal{L}^{(6)}_{HVV}$ is momentum dependent in the momentum representation, i.e., the dim-6 coupling has an extra factor of $O(k^2/\Lambda^2)$ relative to the dim-4 coupling. This means that the effect of $\mathcal{L}^{(6)}_{HVV}$ is small in the low momentum region but it is enhanced in high energy

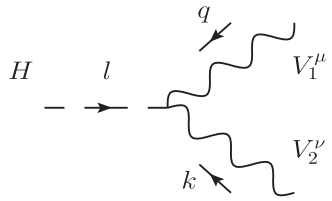

FIG. 1. Illustration of the momenta in the HVV interactions in Eq. (10).

processes. This is the reason why we take into account both $\mathcal{L}^{(4)}_{HVV}$ and $\mathcal{L}^{(6)}_{HVV}$ in our study.

To see the details of the momentum dependence, we list, in the following, the momentum representations of the HVV interactions in (10).

The three momenta in the HVV vertices in (10) are illustrated in Fig. 1, in which l stands for the momentum of H, and q and k stand for the momenta of the two gauge fields V_1^μ and V_2^ν, respectively. They satisfy

$$l_\mu + q_\mu + k_\mu = 0. \tag{12}$$

(a) The $H\gamma\gamma$ interactions

$$\begin{aligned} g_{H\gamma\gamma} H A_{\mu\nu} A^{\mu\nu} &\to 2 g_{H\gamma\gamma}(q_\nu k_\mu - g_{\mu\nu} q\cdot k) A^\mu A^\nu H \\ &= -2 g M_W \rho_H \frac{s^2(f_{BB}+f_{WW})}{2\Lambda^2} \\ &\quad \times (q_\nu k_\mu - g_{\mu\nu} q\cdot k) A^\mu A^\nu H \end{aligned} \tag{13}$$

(b) The $HZ\gamma$ interactions

Taking $V_1^\mu = A^\mu$, $V_2^\mu = Z^\mu$, we have

$$\begin{aligned} & g^{(1)}_{HZ\gamma} A_{\mu\nu} Z^\mu \partial^\nu H + g^{(2)}_{HZ\gamma} H A_{\mu\nu} Z^{\mu\nu} \\ &\to [g^{(1)}_{HZ\gamma}(q_\mu q_\nu - q^2 g_{\mu\nu} + q_\nu k_\mu - g_{\mu\nu} q\cdot k) \\ &\quad + 2 g^{(2)}_{HZ\gamma}(q_\nu k_\mu - g_{\mu\nu} q\cdot k)] A^\mu Z^\nu H \\ &= \frac{g M_W \rho_H s}{2 c \Lambda^2}[(f_W - f_B)(q_\mu q_\nu - q^2 g_{\mu\nu}) + (f_W - f_B \\ &\quad + 4(s^2 f_{BB} - c^2 f_{WW}))(q_\nu k_\mu - g_{\mu\nu} q\cdot k)] A^\mu Z^\nu H. \end{aligned} \tag{14}$$

Neglecting the small term proportional to s^2, we have

$$\begin{aligned} & g^{(1)}_{HZ\gamma} A_{\mu\nu} Z^\mu \partial^\nu H + g^{(2)}_{HZ\gamma} H A_{\mu\nu} Z^{\mu\nu} \\ &\approx \frac{g M_W \rho_H s}{2 c \Lambda^2}[(f_W - f_B)(q_\mu q_\nu - q^2 g_{\mu\nu}) \\ &\quad + (f_W - f_B - 4 f_{WW})(q_\nu k_\mu - g_{\mu\nu} q\cdot k)] A^\mu Z^\nu H. \end{aligned} \tag{15}$$

(c) The HWW interactions

$$\begin{aligned} & g^{(1)}_{HWW}(W^+_{\mu\nu} W^{-\mu} \partial^\nu H + \text{H.c.}) + g^{(2)}_{HWW} H W^+_{\mu\nu} W^{-\mu\nu} \\ &\to [g^{(1)}_{HWW}(q_\mu q_\nu - q^2 g_{\mu\nu} + k_\mu k_\nu - k^2 g_{\mu\nu}) \\ &\quad + 2(g^{(1)}_{HWW} + g^{(2)}_{HWW})(q_\nu k_\mu - q\cdot k g_{\mu\nu})] W^{+\mu} W^{-\nu} H \\ &= \frac{g M_W \rho_H}{2\Lambda^2}[f_W(q_\mu q_\nu - q^2 g_{\mu\nu} + k_\mu k_\nu - k^2 g_{\mu\nu}) \\ &\quad + 2(f_W - 2 f_{WW})(q_\nu k_\mu - q\cdot k g_{\mu\nu})] W^{+\mu} W^{-\nu} H \end{aligned} \tag{16}$$

(d) The HZZ interactions

$$\begin{aligned} & g^{(1)}_{HZZ} Z_{\mu\nu} Z^\mu \partial^\nu H + g^{(2)}_{HZZ} H Z_{\mu\nu} Z^{\mu\nu} \\ &\to \left[\frac{1}{2} g^{(1)}_{HZZ}(q_\mu q_\nu - q^2 g_{\mu\nu} + k_\mu k_\nu - k^2 g_{\mu\nu}) \right. \\ &\quad \left. + (g^{(1)}_{HZZ} + 2 g^{(2)}_{HZZ})(q_\nu k_\mu - g_{\mu\nu} q\cdot k)\right] Z^\mu Z^\nu H \\ &= \frac{g M_W \rho_H}{2 c^2 \Lambda^2}\left[\frac{1}{2}(c^2 f_W + s^2 f_B)\right. \\ &\quad \times (q_\mu q_\nu - q^2 g_{\mu\nu} + k_\mu k_\nu - k^2 g_{\mu\nu}) \\ &\quad + (c^2 f_W + s^2 f_B - 2 s^4 f_{BB} - 2 c^4 f_{WW}) \\ &\quad \left. \times (q_\nu k_\mu - g_{\mu\nu} q\cdot k)\right] Z^\mu Z^\nu H \end{aligned} \tag{17}$$

Neglecting the small terms proportional to s^2 and s^4, we have

$$\begin{aligned} & g^{(1)}_{HZZ} Z_{\mu\nu} Z^\mu \partial^\nu H + g^{(2)}_{HZZ} H Z_{\mu\nu} Z^{\mu\nu} \\ &\approx \frac{g M_W \rho_H}{2 c^2 \Lambda^2}\left[\frac{1}{2} f_W(q_\mu q_\nu - q^2 g_{\mu\nu} + k_\mu k_\nu - k^2 g_{\mu\nu}) \right. \\ &\quad \left. + (f_W - 2 f_{WW})(q_\nu k_\mu - g_{\mu\nu} q\cdot k)\right] Z^\mu Z^\nu H. \end{aligned} \tag{18}$$

Now the gauge boson masses, especially the W boson mass, are also contributed to by more than one Higgs fields. Since $\mathcal{L}^{(6)}_{HVV}$ contains extra derivatives, it does not contribute to the W boson mass. From (5) and (6) we see that

$$\begin{aligned} M_W^2 &= \frac{1}{4}(g_h^2 v_h^2 + g_H^2 v_H^2 + \cdots\cdots) \\ &= \frac{1}{4} g^2 v(\rho_h v_h + \rho_H v_H + \cdots\cdots). \end{aligned} \tag{19}$$

Comparing with the SM W boson mass $M_W^2 = g^2 v^2/4$, we obtain

$$\rho_h \frac{v_h}{v} + \rho_H \frac{v_H}{v} + \cdots\cdots = 1. \tag{20}$$

This serves as another constraint on the gauge coupling constants and VEVs. It is easy to see that the two constraints (20) and (4) can be satisfied simultaneously.

III. UNITARITY CONSTRAINTS ON THE ANOMALOUS COUPLING CONSTANTS

As we mentioned in the last section, the anomalous interactions in $\mathcal{L}^{(4)}_{HVV}+\mathcal{L}^{(6)}_{HVV}$ include five unknown anomalous coupling constants ρ_H, f_W, f_{WW}, f_B, and f_{BB}. Low energy observables are insensitive to the related operators in $\mathcal{L}^{(6)}_{HVV}$. We are going to study certain constraints from high energy processes. In this section, we study the theoretical constraint obtained from the requirement of the unitarity of the S matrix. In the next section, we shall study the experimental constraint obtained from the CMS 95% C.L. exclusion bound on the SM Higgs boson.

We would like to emphasize that we are not aiming at precision calculations in this and the next sections. Instead, our purpose is to find out a rough range of the anomalous coupling constants f_W and f_{WW} with f_W and f_{WW} inside which the heavy Higgs boson is not excluded by the existing theoretical and experimental constraints, so that the study of probing the heavy Higgs boson at 14 TeV LHC makes sense.

Since the operators in $\mathcal{L}^{(6)}_{HVV}$ are momentum dependent, it will violate the unitarity of the S matrix at high energies (note that the CM energy can not exceed Λ in the effective Lagrangian theory). So the requirement of the unitarity of the S matrix can give constraints on the size of the anomalous coupling constants. This kind of study has been given in several papers [23] in which the effective couplings for the single-Higgs system were taken, and the study is a single-parameter analysis. We cannot simply take such a constraint in our study because we are studying the effective couplings in a multi-Higgs system taking account of the contributions of both the lightest SM-like Higgs h and a heavier neutral Higgs boson H with ρ_h, $\rho_H \neq 1$. In the following, to get the order of magnitude constraints, we study the unitarity constraints for our case in the effective W approximation.

The strongest constraints come from the longitudinal weak-boson scattering since the polarization vector ϵ^μ_L of W_L (Z_L) contains extra momentum dependence. To the precision of effective W approximation, it is reasonable to neglect the small terms of $O(s^2)$ and $O(s^4)$ in the anomalous HZZ coupling as in the last step in Eq. (18). Then we see from (16) and (18) that the relevant anomalous HWW and HZZ couplings contain only three unknown coupling constants ρ_H, f_W, and f_{WW}, irrelevant to f_B and f_{BB}.

Expressing the S matrix by $S=1-iT$, the unitarity of the S matrix reads

$$|S^\dagger S| = |1-iT|^2 = 1 \tag{21}$$

which leads to the following requirement:

$$\begin{aligned}&(\mathrm{Re}\langle a|T|a\rangle)^2+(\mathrm{Im}\langle a|T|a\rangle-1)^2+\sum_{|b\rangle\neq|a\rangle}|\langle b|T|a\rangle|^2=1\\ &\Rightarrow (\mathrm{Re}\langle a|T|a\rangle)^2+\sum_{|b\rangle\neq|a\rangle}|\langle b|T|a\rangle|^2\leq 1.\end{aligned} \tag{22}$$

When we take $|a\rangle=|W_LW_L\rangle$, the leading final state $\langle b|$ is $\langle W_LW_L|$ and $\langle Z_LZ_L|$. In certain regions of the anomalous coupling constants, the leading matrix element may be small, so that other nonleading final states should also be considered. Thus, we also include $\langle b|=\langle W_TW_T|$, and $\langle Z_TZ_T|$. Similarly, when we take $|a\rangle=|Z_LZ_L\rangle$, we take $\langle b|=\langle Z_LZ_L|$, $\langle W_TW_T|$, and $\langle Z_TZ_T|$.

As usual, the unitarity constraints are to be calculated in the partial wave expression which was studied in detail in Ref. [24]. It is well known that the S-wave contribution is dominant. So we only calculate the matrix elements of the S-wave amplitude T^0. For $|a\rangle=|W_LW_L\rangle$ and $|a\rangle=|Z_LZ_L\rangle$, the unitarity constraints read

$$\begin{aligned}&|\mathrm{Re}\langle W_L^+W_L^-|T^0|W_L^+W_L^-\rangle|^2+|\langle Z_LZ_L|T^0|W_L^+W_L^-\rangle|^2\\ &+2|\langle W_+^+W_+^-|T^0|W_L^+W_L^-\rangle|^2+2|\langle Z_+Z_+|T^0|W_L^+W_L^-\rangle|^2\\ &\leq 1,\end{aligned} \tag{23}$$

and

$$\begin{aligned}&|\mathrm{Re}\langle Z_LZ_L|T^0|Z_LZ_L\rangle|^2+2|\langle Z_\pm Z_\pm|T^0|Z_LZ_L\rangle|^2\\ &+|\langle W_L^+W_L^-|T^0|Z_LZ_L\rangle|^2+2|\langle W_\pm^+W_\pm^-|T^0|Z_LZ_L\rangle|^2\\ &\leq 1.\end{aligned} \tag{24}$$

In our study, we have taken into account the contributions of both h and H. These kinds of results have not been given in the published papers. We shall present our analytical results and numerical analysis as follows. We give the results in the center-of-mass frame, and express the scattering amplitudes in terms of the s, t, u parameters.

A. $W_L^+W_L^- \to VV$

$$\begin{aligned}&\mathrm{Re}\langle W_L^+W_L^-|T^0|W_L^+W_L^-\rangle\\ &=-\frac{g^2}{64\pi}\left\{\left[\rho_H^2\left(1-\frac{M_W^2}{\Lambda^2}f_W\right)^2+\rho_h^2-1\right]\frac{\mathsf{s}}{M_W^2}+O(\mathsf{s}^0)\right\}.\end{aligned} \tag{25}$$

$$\begin{aligned}\langle Z_LZ_L|T^0|W_L^+W_L^-\rangle=&\frac{g^2}{32\pi}\left\{\left[\rho_H^2\left(1-\frac{M_W^2}{\Lambda^2}f_W\right)\left(\frac{M_Z^2}{\Lambda^2}f_W-1\right)\right.\right.\\ &\left.\left.-\rho_h^2+1\right]\frac{\mathsf{s}}{M_W^2}+O(\mathsf{s}^0)\right\}.\end{aligned} \tag{26}$$

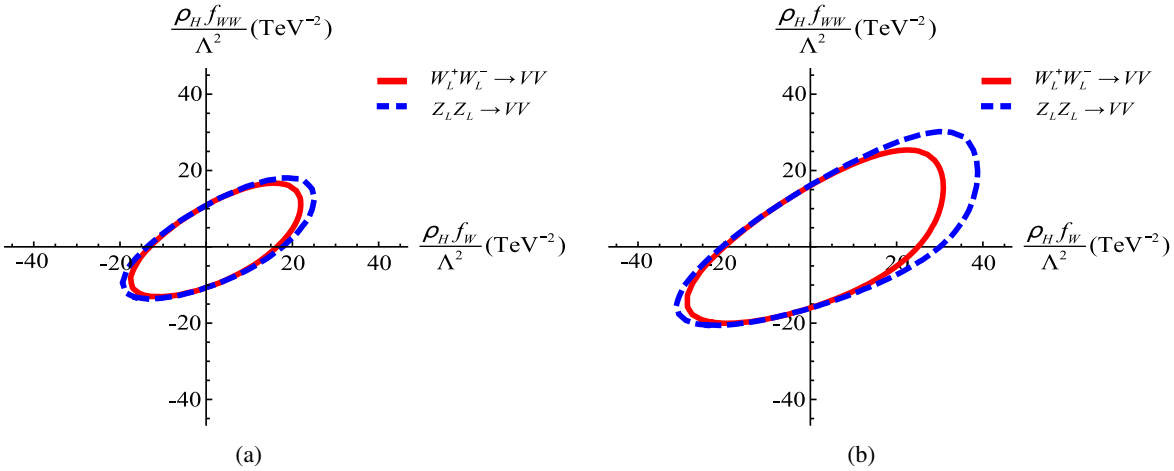

FIG. 2 (color online). Unitarity bounds on f_W and f_{WW} in which (a) is with $\rho_h = 0.8$ and $\rho_H = 0.6$; (b) is with $\rho_h = 0.9$ and $\rho_H = 0.4$. The red and blue-dashed contours are boundaries of the allowed regions obtained from $W_L^+W_L^- \to VV$ [Eq. (23)] and $Z_LZ_L \to VV$ [Eq. (24)], respectively.

$$\langle W_\pm^+ W_\pm^- | T^0 | W_L^+ W_L^- \rangle = \frac{\rho_H^2 g^2}{32\pi}\left(1 - \frac{M_W^2}{\Lambda^2} f_W\right)(2f_{WW} - f_W)\frac{\mathsf{s}}{\Lambda^2} + O(\mathsf{s}^0). \quad (27)$$

$$\langle Z_\pm Z_\pm | T^0 | W_L^+ W_L^- \rangle = \frac{\rho_H^2 g^2}{32\pi}\left(1 - \frac{M_W^2}{\Lambda^2} f_W\right)(2f_{WW} - f_W)\frac{\mathsf{s}}{\Lambda^2} + O(\mathsf{s}^0). \quad (28)$$

In (25)–(28), the terms with ρ_H are the contributions of H, and those with ρ_h are contributions of h. We see from (27) and (28) that, in these two matrix elements, the leading terms contain only the contributions of H (from its dim-6 couplings).

B. $Z_LZ_L \to VV$

Since there are all s, t and u channel contributions in $Z_LZ_L \to Z_LZ_L$, the leading $O(\mathsf{s}^1)$ terms in the three channels just cancel with each other. So

$$\text{Re}\langle Z_LZ_L | T^0 | Z_LZ_L \rangle = O(\mathsf{s}^0). \quad (29)$$

Results of other final states are

$$\langle Z_\pm Z_\pm | T^0 | Z_LZ_L \rangle = \frac{\rho_H^2 g^2}{32\pi}\left\{\left(1 - \frac{M_Z^2}{\Lambda^2} f_W\right) \times (2f_{WW} - f_W)\frac{\mathsf{s}}{\Lambda^2} + O(\mathsf{s}^0)\right\}, \quad (30)$$

and

$$\langle W_\pm^+ W_\pm^- | T^0 | Z_LZ_L \rangle = \frac{\rho_H^2 g^2}{32\pi}\left\{(2f_{WW} - f_W)\left(1 - \frac{M_Z^2}{\Lambda^2} f_W\right) \times \frac{\mathsf{s}}{\Lambda^2} + O(\mathsf{s}^0)\right\}. \quad (31)$$

We see that in (29)–(31), all the leading terms contain only the contributions of H (from its dim-6 couplings).

With all the above results, we are ready to analyze the unitarity constraints on the anomalous coupling constants f_W and f_{WW}. Since we are interested in weak-boson scattering at high energies in which $\mathcal{L}_{HVV}^{(6)}$ is enhanced, we shall only keep the terms with leading power of s in all the above results. In our numerical analysis, we simply take the s parameter to be its highest value $\mathsf{s} = \Lambda^2$. We shall study such constraints numerically performing a two-parameter analysis. Before doing that, we need to specify the other unknown parameters. First of all, as we have mentioned in Sec. II, we shall take $\Lambda = 3$ TeV as an example. For ρ_h, the known SM-like properties of h means that ρ_h should not be so different from 1. We shall take $\rho_h = 0.8, 0.9$ as two examples. For ρ_H, we shall see in the next section that if $\rho_H > 0.6$, the heavy neutral Higgs boson H can hardly avoid being excluded by the CMS 95% C.L. exclusion bounds on the SM Higgs boson. Therefore, for an existing H, ρ_H should be less than 0.6. We shall take $\rho_H = 0.6, 0.4$ as two examples. The results of our analysis are shown in Fig. 2 in which Fig. 2(a) is with $\rho_h = 0.8$, $\rho_H = 0.6$, and Fig. 2(b) is with $\rho_h = 0.9$, $\rho_H = 0.4$. In Fig. 2, the red and blue-dashed contours are boundaries of the allowed regions obtained from $W_L^+W_L^- \to VV$ [Eq. (23)] and $Z_LZ_L \to VV$ [Eq. (24)], respectively.

We see that $\rho_H f_W/\Lambda^2$ and $\rho_H f_{WW}/\Lambda^2$ are constrained up to a few tens of TeV^{-2} which is different from the results given in Ref. [23].

So far we have not concerned the unitarity bounds on f_B and f_{BB}. In principle, they can be obtained by studying the scattering processes $W_L W_L \to \gamma\gamma$ and $W_L W_L \to Z\gamma$. However, since the photon has only transverse polarizations, such bounds will be weaker. Actually, in the next section, we shall argue that we may make the approximation of neglecting the anomalous coupling constants in the dim-6 couplings of the $H\gamma\gamma$ and $HZ\gamma$ couplings.

IV. EXPERIMENTAL CONSTRAINTS ON ANOMALOUS COUPLING CONSTANTS

After the discovery of the 125–126 GeV Higgs boson in 2012, the CMS (ATLAS) Collaboration has made a lot of measurements on excluding the SM Higgs boson with mass up to 1 TeV (600 GeV) [1,10,25] at 95% C.L. For a NS heavy neutral Higgs boson, it must have large enough anomalous couplings to reduce its production cross section to avoid being excluded by the CMS experiments. This provides the possibility of constraining the anomalous coupling constants experimentally. In this section, we study such experimental bounds. Values of the anomalous coupling constants consistent with both the unitarity constraint and the experimental constraint are the *available* anomalous coupling constants that an existing heavy neutral Higgs boson can have.

Unlike what we did in the last section, we take account here of the Higgs decay rates and the Higgs width to full leading order in perturbation, and we keep the nonvanishing weinberg angle, i.e., we use (14) and (17) rather than (15) and (18) for $\mathcal{L}^{(6)}_{HZ\gamma}$ and $\mathcal{L}^{(6)}_{HZZ}$. In our numerical analysis, we take FeynRules 2.0 [26] in our analysis code, and we use MADGRAPH5 [27] to calculate the Higgs production and decay rates.

In our effective couplings, there are altogether seven unknown parameters, namely, $C_t, \rho_h, \rho_H, f_W, f_{WW}, f_B$, and f_{BB}. So the analysis is rather complicated. From Eq. (11), we see that f_B and f_{BB} do not appear in the HWW vertex, and they appear in the HZZ vertex with the suppression factors s^2 and s^4, respectively. So their contributions to VV scattering and $pp \to VH^* \to VVV$ studied in our next paper are negligibly small. They are mainly related to the decays $H \to \gamma\gamma$ and $H \to Z\gamma$. However, for the heavy Higgs boson with $M_H \geq 400$ GeV in our study, all the decay channels $H \to WW$, $H \to ZZ$ and $H \to t\bar{t}$ are open, so that the two decay channels $H \to \gamma\gamma$ and $H \to Z\gamma$ are relatively not so important. Since we are not aiming at doing precision calculations, we may take a certain approximation to avoid dealing with f_B and f_{BB} in the analysis to simplify it.

We then examine the ATLAS and CMS results of the strength $\mu = \sigma/\sigma_{\rm SM}|_{95\%\ \rm C.L.}$ for the decay channels $H \to \gamma\gamma$ [28,29] and $H \to Z\gamma$ [30,31]. Unfortunately, the data only exist below 150 GeV which does not include the range $M_H \geq 400$ GeV in our study. So we can only make a speculation of the situation in the range above 150 GeV. We see from the results in Refs. [28–31] that the trend of the ATLAS and CMS results below 150 GeV is that the experimental curves tend to gradually go closer to the $\mu = 1$ axis. So we roughly estimate that they may keep this situation above 150 GeV. This means that there is no evidence of needing significant anomalous couplings in the $H\gamma\gamma$ and $HZ\gamma$ couplings, i.e., we just neglect the anomalous coupling constants of the effective $H\gamma\gamma$ and $HZ\gamma$ interactions. We first see from Eq. (13) that neglecting the anomalous coupling constant in Eq. (13) means

$$f_{BB} \approx -f_{WW}. \tag{32}$$

We then see from Eq. (14) that there are two terms in it. The first term is proportional to $(q_\mu q_\nu - q^2 g_{\mu\nu})A^\mu$ which vanishes for the on-shell photon. Thus, neglecting the anomalous coupling constant in Eq. (14) means

$$f_B \approx f_W - 4f_{WW}. \tag{33}$$

Equations (32) and (33) serve as two constraints on f_{BB} and f_B, expressing them in terms of f_W and f_{WW}. Then we have only five unknown coupling constants left, namely, C_t, ρ_h, ρ_H, f_W, and f_{WW}, as in the last section.

Next we look at $\mathcal{L}^{(6)}_{HWW}$ and $\mathcal{L}^{(6)}_{HZZ}$. We see from (16) that $\mathcal{L}^{(6)}_{HWW}$ does not contain f_B and f_{BB}, so it is unaffected by the approximations (32) and (33). However, $\mathcal{L}^{(6)}_{HZZ}$ does contain f_B and f_{BB}. With the approximations (32) and (33), Eq. (17) becomes

$$\begin{aligned}\mathcal{L}^{(6)}_{HZZ} = \frac{gM_W\rho_H}{2c^2\Lambda^2}\Big[&\frac{1}{2}(f_W - 4s^2 f_{WW}) \\ &\times (q_\mu q_\nu - q^2 g_{\mu\nu} + k_\mu k_\nu - k^2 g_{\mu\nu}) \\ &+ (f_W - 2f_{WW})(q_\nu k_\mu - g_{\mu\nu} q\cdot k)\Big] Z^\mu Z^\nu H.\end{aligned} \tag{34}$$

Now we consider the CMS and ATLAS exclusion bounds on SM Higgs boson [1,10,25]. The strongest one is the CMS result obtained from the $H \to ZZ \to 4\ell$ channel [10]. In this section, we mainly consider this strongest bound, and we also take account of other weaker bounds [25] when considering the size of the available range for f_W and f_{WW}.

The strongest CMS exclusion bound is given in the Higgs mass range up to 1 TeV. Its feature is that the experimental curve goes rapidly away from the $\mu = 1$ axis (below $\mu = 1$) above 120 GeV, and fluctuates in the range between 140 and 400 GeV, and then goes relatively smoother towards the $\mu = 1$ axis up to 1 TeV. In view of the significant fluctuations below 400 GeV, we shall take $M_H = 400$, 500, and 800 GeV as examples to do the two-parameter analysis. The parameters in these examples are

(i) 400II: M_H=400 GeV, C_t=0.5 (type II), ρ_h=0.9, $\rho_H = 0.4$,
(ii) 500I: M_H=500 GeV, $C_t = 1$ (type I), $\rho_h = 0.9$, $\rho_H = 0.4$,
(iii) 500II: $M_H = 500$ GeV, $C_t = 0.6$ (type II), $\rho_h = 0.8$, $\rho_H = 0.6$,
(iv) 800I: $M_H = 800$ GeV, $C_t = 1$ (type I), $\rho_h = 0.8$, $\rho_H = 0.6$,
(v) 800II: $M_H = 800$ GeV, $C_t = 0.2$ (type II), $\rho_h = 0.9$, $\rho_H = 0.25$.

When calculating the strength μ for $H \to ZZ \to 4\ell$, we need to calculate

$$\sigma = \sigma(pp \to HX)B(H \to ZZ \to 4\ell),$$
$$B(H \to ZZ \to 4\ell) = \frac{\Gamma(H \to ZZ \to 4\ell)}{\Gamma(H \to ZZ) + \Gamma(H \to WW) + \cdots}. \quad (35)$$

The total decay width $\Gamma(H \to ZZ) + \Gamma(H \to WW) + \cdots$ needs further discussion. Apart from the decay modes related to the effective coupling mentioned in Sec. II, there can also be the decay mode $H \to hh$ caused by an effective coupling $\lambda v_H Hhh$ (note that H is the lightest heavy Higgs boson so that it can not decay to other heavy Higgs bosons). For H with $M_H \geq 400$ GeV, all the decay channels $H \to WW$, $H \to ZZ$ and $H \to t\bar{t}$ are open. Since M_h is larger than M_W and M_Z, the phase space in $H \to hh$ is smaller than those in $H \to WW$ and $H \to ZZ$. Thus the mode $H \to hh$ does not play an important role in the total width. Since we are not aiming at doing precision calculations, we can make the approximation of neglecting the $H \to hh$ mode in the total decay width of H to avoid introducing a new unknown parameter λ. In this approximation, our obtained total decay width of H is smaller than its actual value. This makes the obtained exclusion constraint on H stronger than what it actually is. Thus our approximate calculation is a conservative calculation, i.e., the required values of f_W and f_{WW} from our approximate exclusion bound are more than enough for avoiding being excluded by the actual exclusion bound. This guarantees that a heavy Higgs boson H with the obtained allowed values of f_W and f_{WW} is definitely not excluded by the CMS exclusion bound [10].

Now we present our two-parameter numerical analysis results.

(1) $M_H = 400$ GeV

As we have mentioned, the exclusion bound is very strong at $M_H = 400$ GeV. Our numerical analysis shows that, for the case of type I, a NS heavy neutral Higgs boson with $M_H = 400$ GeV can hardly avoid being excluded. Of course, if we take ρ_H to be small enough, it may help. But a heavy neutral Higgs boson with so small gauge interactions is not considered in this study, and will be considered elsewhere.

Now we consider the case of 400II. The small C_t reduces the Higgs production cross section by gluon fusion $\sigma(pp \to HX)$, so that the requirement of reducing $B(H \to ZZ \to 4\ell)$ is milder, and it is possible to find out the available values of f_W and f_{WW}. The result of our two-parameter numerical analysis is shown in Fig. 3. The shaded region means the values of f_W and f_{WW} which can sufficiently reduce the branching ratio $B(H \to ZZ \to 4\ell)$ such that the heavy neutral Higgs boson is not excluded by the CMS exclusion bound. Considering further the unitarity bound in Fig. 2(b), we find that the real available region (consistent with the unitarity bound) is the part shaded in blue.

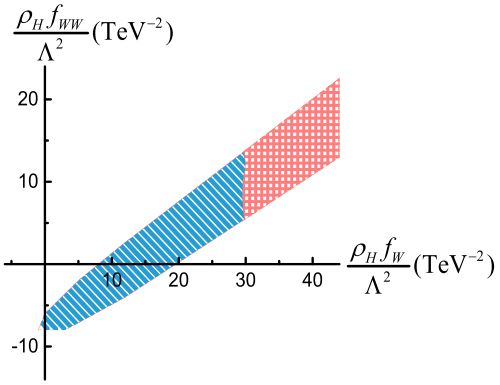

FIG. 3 (color online). Obtained experimental bound on f_W and f_{WW} in the case of 400II. The blue shaded region is the available region.

(2) $M_H = 500$ GeV

For $M_H = 500$ GeV, the SM Higgs exclusion bound is looser. We take two sets of parameters as examples, namely, 500I (type I) case with $C_t = 1$, $\rho_h = 0.9$, $\rho_H = 0.4$; and 500II (type II) case with $C_t = 0.6$, $\rho_h = 0.8$, $\rho_H = 0.6$.

We first look at the 500I case. The result of our two-parameter numerical analysis is shown in Fig. 4 in which the shaded region is the region of f_W and f_{WW}, making the heavy neutral Higgs boson H not excluded by the CMS exclusion bound, and the small part shaded in blue is consistent with the unitarity bound shown in Fig. 2(b), i.e., the available region. Note that this is also in the first quadrant of the f_W-f_{WW} plane.

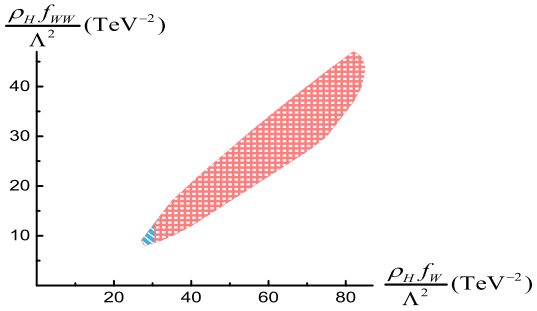

FIG. 4 (color online). Obtained experimental bound on f_W and f_{WW} in the case of 500I. The blue shaded region is the available region.

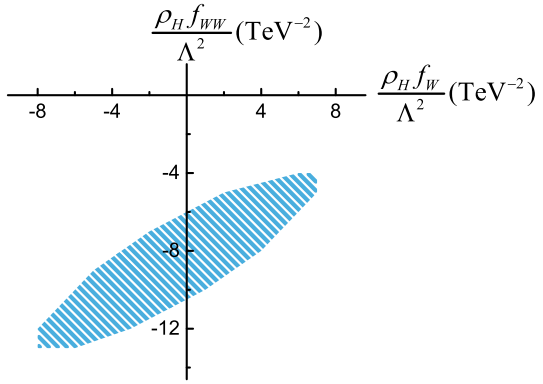

FIG. 5 (color online). Obtained experimental bound on f_W and f_{WW} in the case of 500II. The blue shaded region is the available region.

Next we look at the 500II case. The result of our two-parameter numerical analysis is shown in Fig. 5 in which the blue shade region is the available region [the whole region is consistent with the unitarity bound shown in Fig. 2(a)]. These available region is in the third and fourth quadrants. Since the value $\rho_H = 0.6$ is larger than that in the 500I case, the needed values of f_W and f_{WW} for sufficiently reducing $B(H \to ZZ \to 4\ell)$ in the first quadrant are so large that they exceed the unitarity bound shown in Fig. 2(a). Thus only the region shown in Fig. 5 is really available.

(3) $M_H = 800$ GeV

We see from the CMS exclusion bound [10] that the exclusion bound at $M_H = 800$ GeV is very loose, so that almost all values of f_W and f_{WW} are available to make the heavy neutral Higgs boson not excluded by the CMS exclusion bound. In the 800I case, $C_t = 1$, the total decay width of the 800 GeV heavy neutral Higgs boson is quite large that it is not possible to see a resonance bump at the LHC, but it is still possible to detect it by measuring the cross section. In the 800II case, a sufficiently small value of C_t will make the total decay width small enough that a resonance bump can be seen at the LHC.

To understand why the available regions in Figs. 3, 4, and 5 are so different, let us look at how f_W and f_{WW} affect $\Gamma(H \to WW)$ and $\Gamma(H \to ZZ)$. Below are our obtained results of $\Gamma(H \to WW)$ and $\Gamma(H \to ZZ)$.

$$\Gamma(H \to WW) \approx \frac{g^2\rho_H^2 M_H^3}{64\pi M_W^2}\left[\left(1 - \frac{M_W^2}{\Lambda^2} f_W\right)^2 + 2\frac{M_W^4}{\Lambda^4}(f_W - 2f_{WW})^2 + O\left(\frac{M_W^2}{M_H^2}\right)\right], \tag{36}$$

$$\Gamma(H \to ZZ) \approx \frac{g^2\rho_H^2 M_H^3}{128\pi M_W^2}\left[\left(1 - \frac{M_Z^2}{\Lambda^2}(f_W - 4s^2 f_{WW})\right)^2 + 2\frac{M_Z^4}{\Lambda^4}(f_W - 2f_{WW})^2 + O\left(\frac{M_W^2}{M_H^2}\right)\right]. \tag{37}$$

First of all, we see from (36) and (37) that, if f_W and f_{WW} are in the second quadrant of the f_W-f_{WW} plane, i.e., $f_W < 0$, $f_{WW} > 0$, they always increase $\Gamma(H \to WW)$ and $\Gamma(H \to ZZ)$, and $\Gamma(H \to ZZ)$ is increased more than $\Gamma(H \to WW)$ is. In this case, $B(H \to ZZ \to 4\ell)$ is always increased, so that the heavy Higgs boson H is definitely excluded by the CMS exclusion bound, i.e., there is no available region of f_W and f_{WW} in the second quadrant of the f_W-f_{WW} plane. It is so in Figs. 3, 4, and 5.

Next we look at the case that $|f_W|, |f_{WW}| < \Lambda^2/M_W^2$ with $f_W - 2f_{WW}$ not too large. We see from (36) and (37) that, for f_W and f_{WW} in the first quadrant ($f_W > 0$, $f_{WW} > 0$), $\Gamma(H \to WW)$ and $\Gamma(H \to ZZ)$ are all decreased, and $\Gamma(H \to WW)$ is decreased more than $\Gamma(H \to ZZ)$ is. So that $B(H \to ZZ \to 4\ell)$ is increased, i.e., there is no available region of f_W and f_{WW} in the first quadrant of the f_W-f_{WW} plane. However, in the third quadrant ($f_W < 0$, $f_{WW} < 0$) and the fourth quadrant ($f_W > 0$, $f_{WW} < 0$), either $\Gamma(H \to WW)$ is increased more than $\Gamma(H \to ZZ)$ is, or $\Gamma(H \to WW)$ is decreased less than $\Gamma(H \to ZZ)$ is. Thus in these two quadrants, $B(H \to ZZ \to 4\ell)$ is reduced, so that there can be an available region of f_W and f_{WW} in the third and fourth quadrants of the f_W-f_{WW} plane. This is just the situation in Fig. 5. In the special case of 400II with $C_t = 0.5$, which significantly reduces the Higgs production cross section $\sigma(pp \to HX)$, in addition to the third and fourth quadrants, there can also be an available region in the first quadrant even if $B(H \to ZZ \to 4\ell)$ is increased a little there. Thus, in this special case, there can be available regions in the first, third, and fourth quadrants. This is the situation in Fig. 3.

We then look at the case that $|f_W|, |f_{WW}| \sim \Lambda^2/M_W^2$. In this case, we should examine both the first and second terms in (36) and (37). In the first quadrant, the first terms are quite small, and the second terms (proportional to $f_W - 2f_{WW}$) can also be small when $f_W \approx 2f_{WW}$, while the total decay rate [the denominator in Eq. (35)] is not reduced so much since $\Gamma(H \to t\bar{t})$ is not so small. So, in this case, $B(H \to ZZ \to 4\ell)$ can be sufficiently reduced. In the fourth quadrant, the second terms are not small enough, and in the third quadrant, the first terms are not small enough. So that in the third and fourth quadrants $B(H \to ZZ \to 4\ell)$ cannot be sufficiently reduced. Thus, in this case there can be an available region of f_W and f_{WW} only in the first quadrant of the f_W-f_{WW} plane. This is the situation in Fig. 4.

When $|f_W|$ and $|f_{WW}|$ become larger and larger, the constant terms (independent of f_W and f_{WW}) in (36) and (37) are less and less important. In this case, $\Gamma(H \to WW)$ and $\Gamma(H \to ZZ)$ all increase, and they are different only by the term containing $4s^2 f_{WW}$. It can be shown that, in this case,

$$\Gamma(H \to ZZ) \not< 0.2\Gamma(H \to WW), \tag{38}$$

or

$$\frac{\Gamma(H \to ZZ)}{\Gamma(H \to WW) + \Gamma(H \to ZZ)} \not< 0.17. \qquad (39)$$

Comparing the corresponding SM values, our detailed analysis shows that, for $M_H = 400$ and 500 GeV, this is not small enough for sufficiently reducing $B(H \to ZZ \to 4\ell)$ to avoid being excluded by the CMS bound in Ref. [10]. Thus, the available values of $|f_W|$ and $|f_{WW}|$ cannot be arbitrarily large. This is why the available regions in Figs. 3, 4, and 5 are all closed regions.

Finally, we would like to add a discussion on whether it is reasonable to simply apply the CMS exclusion bound to our examples with new physics interactions as what we did above. We know that the detection efficiency of the detector depends on specific interactions, and the detection efficiency of the CMS exclusion bound in Ref. [10] is for the SM interaction. We shall take 400II with $\rho_H f_W/\Lambda^2 = 30\ \text{TeV}^{-2}$ and $\rho_H f_{WW}/\Lambda^2 = 10\ \text{TeV}^{-2}$, 500I with $\rho_H f_W/\Lambda^2 = 30\,\text{TeV}^{-2}$ and $\rho_H f_{WW}/\Lambda^2 = 10\,\text{TeV}^{-2}$, and 500II with $\rho_H f_W/\Lambda^2 = 6\,\text{TeV}^{-2}$ and $\rho_H f_{WW}/\Lambda^2 = -5\,\text{TeV}^{-2}$ as examples to calculate how much their detection efficiencies deviate from that with the SM interaction.

We shall make a calculation to study how much such deviations actually are in detecting $pp \to H \to ZZ \to \ell^+\ell^-\ell^+\ell^-$ at the 8 TeV LHC. We use DELPHES 3 [32] to roughly simulate the detector. We use MADGRAPH5 to do the simulation, and use MadAnalysis to obtain the efficiency.

In our calculation, we have chosen $60\ \text{GeV} < M(\ell^+\ell^-) < 120\ \text{GeV}$ to guarantee that the two final states ℓ^+ and ℓ^- are from the decay of a Z boson. We have also chosen $200\ \text{GeV} < M(\ell^+\ell^-\ell^+\ell^-) < 600\ \text{GeV}$ and $300\ \text{GeV} < M(\ell^+\ell^-\ell^+\ell^-) < 700\ \text{GeV}$ to guarantee the final states $\ell^+\ell^-\ell^+\ell^-$ are from the decay of our heavy Higgs bosons under consideration.

The obtained detection efficiency for detecting $H \to ZZ \to \ell^+\ell^-\ell^+\ell^-$ is listed in Table I.

We see that, for 400II, the new interaction causes a relative change of the efficiency with respect to the SM efficiency by $(17.9\%–17.6\%)/17.6\% = 2\%$. For 500I and 500II, the corresponding relative changes of the efficiency are $(18.6\%–17.6\%)/17.6\% = 6\%$ and $(18.8\%–17.6\%)/17.6\% = 7\%$, respectively. Since we are not aiming at doing precision calculations, a few percent change will not affect our main conclusions in simply applying the CMS exclusion bound to our examples.

V. GENERAL FEATURES OF STUDYING THE LHC SIGNATURES OF H

For the study of the LHC signatures of H at the 14 TeV LHC, we do not suggest taking the conventional on-shell Higgs production, used in studying the properties of the 125–126 GeV Higgs boson, to probe the anomalous heavy Higgs boson. The reason is the following. Comparing Eq. (10) with Eq. (6) in Sec. II, we see that the dim-6 interaction contains an extra factor k^2/Λ^2 relative to the dim-4 interaction, coming from the extra derivatives in Eq. (10). Here k is a typical momentum of the order of the momentum of the Higgs boson. In the on-shell Higgs production, $k^2 \sim M_H^2$. Taking $M_H = 500$ GeV as an example, $k^2/\Lambda^2 \sim M_H^2/\Lambda^2 = 0.25/9 = 0.03$. Thus, the contribution of the dim-6 interaction is only a very tiny portion of the total contribution, so that it is hard to detect the dim-6 interaction effect in the on-shell Higgs production.

Instead, in this paper, we suggest taking VV scattering and $pp \to VH^* \to VVV$ as sensitive processes for probing the anomalous heavy Higgs boson at the 14 TeV LHC. These processes contain off-shell heavy Higgs contributions. In the tail with energy higher than the resonance peak, k^2/Λ^2 can be larger. Although the tail with much higher energy than the resonance is seriously suppressed by the parton distribution (e.g., the region $k^2 \lesssim \Lambda^2$ is almost completely suppressed), the remaining high energy tail can still enhance the contribution of the dim-6 interaction as we shall see in Secs. VI–VIII. Furthermore, each of these two processes contains two HVV vertices. This makes the cross sections more sensitive to the anomalous couplings than in the on-shell Higgs production.

Although the two suggested processes are weak-interaction processes with not so large cross sections, the signal to background ratio can be effectively improved by imposing a series of proper cuts. So the integrated luminosity needed for 3σ and 5σ deviations are not so high (e.g., see Table VI) in Sec. VII.

That weak-boson scattering can be a sensitive process for detecting an anomalous Higgs boson at the LHC was first pointed out in Ref. [20], in which the effective couplings for a single-Higgs system and the pure leptonic decay mode of the final state W bosons were considered. It showed that the required integrated luminosity was high. Reference [33] studied the same problem but with the semileptonic decay channel (one of the final state W boson decays to leptons and the other W boson decays to jets), and showed that the required integrated luminosity was significantly reduced.

TABLE I. Comparison of the detection efficiencies between the SM and our examples: 400II with $\rho_H f_W/\Lambda^2 = 30\ \text{TeV}^{-2}$ and $\rho_H f_{WW}/\Lambda^2 = 10\ \text{TeV}^{-2}$, 500I with $\rho_H f_W/\Lambda^2 = 30\ \text{TeV}^{-2}$ and $\rho_H f_{WW}/\Lambda^2 = 10\ \text{TeV}^{-2}$, and 500II with $\rho_H f_W/\Lambda^2 = 6\ \text{TeV}^{-2}$ and $\rho_H f_{WW}/\Lambda^2 = -5\ \text{TeV}^{-2}$.

	400II	SM ($M_H = 400$ GeV)	500I	500II	SM ($M_H = 500$ GeV)
Detection efficiency	17.9%	17.7%	18.6%	18.8%	17.6%

TABLE II. The detector acceptance.

	$\lvert\eta\rvert_{\max}$	$P_{T\min}$
μ	2.4	10 GeV
e	2.5	10 GeV
Jet	5	20 GeV
Photon	2.5	0.5 GeV

Thus, we shall study the semileptonic decay mode in both the weak-boson scattering and $pp \to VH^* \to VVV$ processes, i.e., $pp \to VVj_1^f j_2^f \to \ell^+\nu_\ell j_1 j_2 j_1^f j_2^f$ (j_1^f, j_2^f stand for forward jets) in weak-boson scattering, and $pp \to VH^* \to VVW \to \ell^+\nu_\ell j_1 j_2 j_3 j_4$ in the $pp \to VH^* \to VVV$ process. Since there are several jets in the final states, parton-level calculation is not adequate. We shall do the calculation to the hadron level.

We take the CTEQ6.1 parton distribution functions [34], and use MADGRAPH5 [27] to do the full tree-level simulation. The parton shower and hadronization are calculated with PYTHIA6.4 [35], and the anti-k_T algorithm [36] in DELPHES 3 [32] is used for the formation of jets with $R = 0.7$ [37]. We also use DELPHES 33 to simulate the detecting efficiency of the detector. We take the five examples in Sec. IV to do the simulation, and take the acceptance of the detector listed in Table II.

In each process, we regard the contributions by the heavy Higgs boson H as the signal, other contributions without H as backgrounds. Among the backgrounds processes, the process with the same initial and final states is regarded as the IB; others are RBs. The signal and the IB should be calculated together since they have interference. Let σ be the total cross section. The background and the signal cross sections are then defined as

$$\sigma_B = \sigma(C_t = 1, \rho_h = 1, \rho_H = 0, f_W = 0, f_{WW} = 0),$$
$$\sigma_S = \sigma - \sigma_B. \tag{40}$$

For an integrated luminosity $\mathsf{L}_{\rm int}$, The signal and background event numbers are $N_S = \mathsf{L}_{\rm int}\sigma_S$, $N_B = \mathsf{L}_{\rm int}\sigma_B$. In this paper, we take the Poisson distribution approach to determine the statistical significance $\sigma_{\rm stat}$. The general Poisson probability distribution reads

$$P_B = \sum_N e^{-N_B}\frac{N_B^N}{N!},$$
$$N = N_S + N_B, N_S + N_B + 1, \cdots, \infty. \tag{41}$$

Comparing the obtained value of $1 - P_B$ with the probability of the signal in the Gaussian distribution, we can find out the corresponding value of $\sigma_{\rm stat}$ [38]. The value of $\sigma_{\rm stat}$ obtained in this way approaches the simple form

$$\sigma_{\rm stat} = \frac{N_S}{\sqrt{N_B}} \tag{42}$$

when N_S and N_B are sufficiently large.

VI. PROBING HEAVY NEUTRAL HIGGS BOSONS VIA WEAK-BOSON SCATTERING

In this section, we study the semileptonic mode of weak-boson scattering, $pp \to VVj_1^f j_2^f \to \ell^+\nu_\ell j_1 j_2 j_1^f j_2^f$. We first

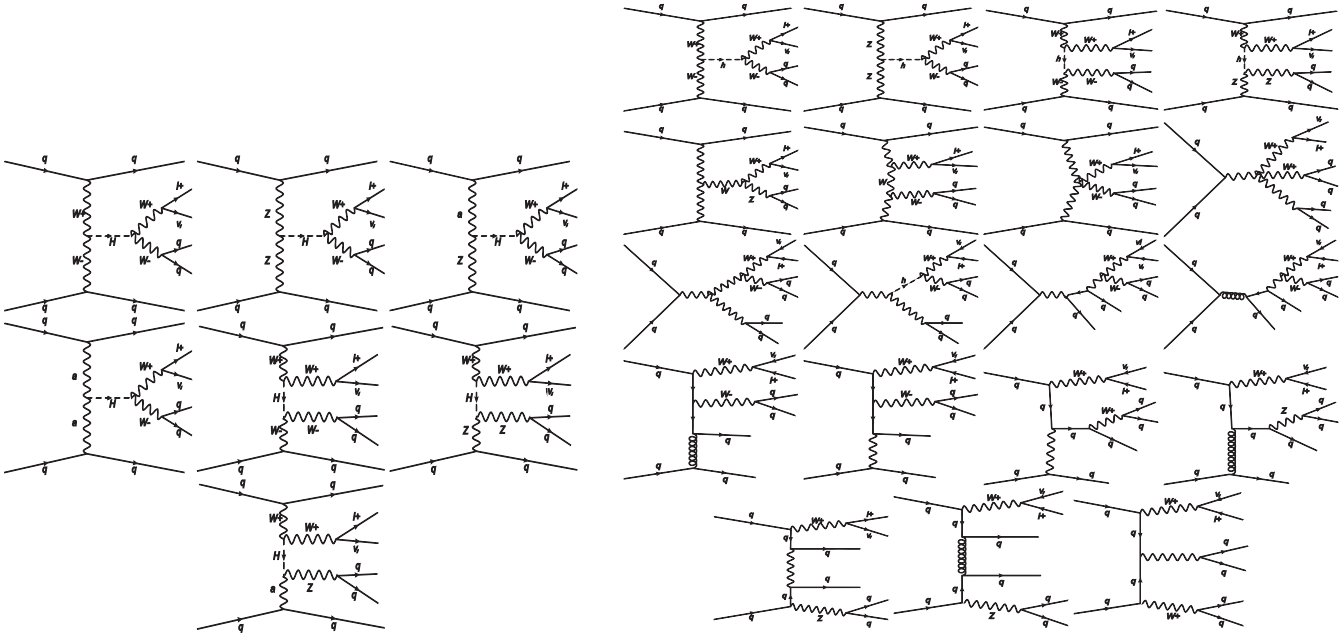

(a) (b)

FIG. 6. Feynman diagrams in weak-boson scattering. (a) The signal, (b) examples of the IB.

look at the Feynman diagrams of the signal, IB, and RBs in this process. Feynman diagrams for the signal and examples of the IB are shown in Fig. 6.

These two kinds of diagrams in Fig. 6(a) and Fig. 6(b) should be calculated together since they have interference.

Apart from the IB, there are two kinds of RBs, namely, the so-called QCD backgrounds and top-quark backgrounds [39]. Note that the two jets j_1 and j_2 from W decay mainly behave as a "single" energetic fat jet J along the W direction [40,41] since the final state W is very energetic. This is the reason why we take $R = 0.7$ in the anti-k_T algorithm. In this case, the important QCD backgrounds which can mimic the signal at the hadron level are the inclusive $W + 3j$ (with $W \to \ell^+\nu_\ell$, and the three jets mimic the fat jet J and the two forward jets) and the $WV + 2j$ (with $W \to \ell^+\nu_\ell$, $V \to J$, and the two jets mimic the two forward jets). The parton-level Feynman diagrams of these two QCD backgrounds are shown in Figs. 7 and 8. These two QCD backgrounds have been discussed in Ref. [33]. In our calculation, we match the partons with jets using the method in Refs. [43,44] to obtain the inclusive $W + 3j$ and inclusive $WV + 2j$ backgrounds.

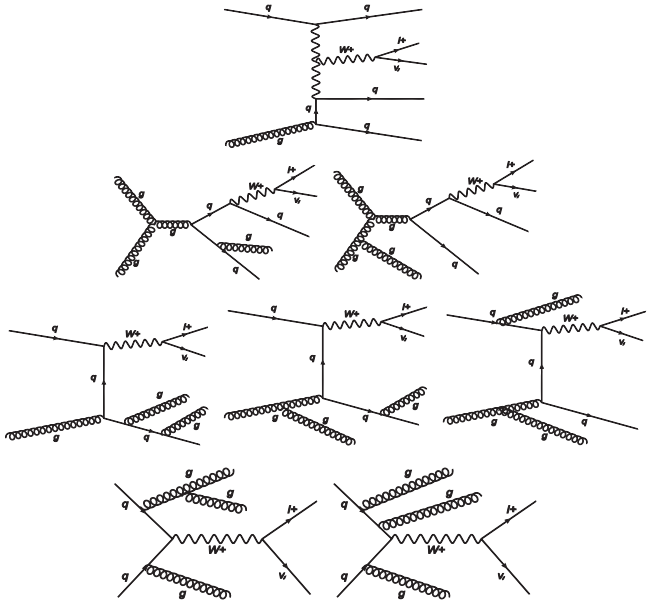

FIG. 7. Feynman diagrams for QCD backgrounds of $W + 3j$.

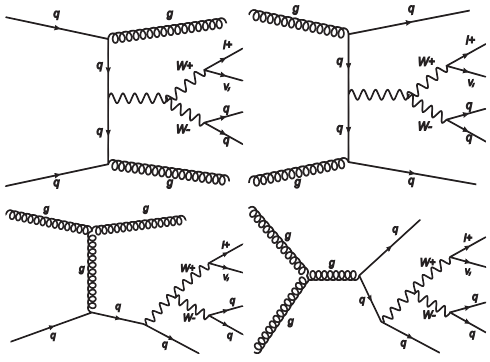

FIG. 8. Feynman diagrams for QCD backgrounds of $WV + 2j$.

The top-quark background is $pp \to t\bar{t} \to W^+bW^-\bar{b} \to \ell^+\nu_\ell j_1 j_2 b\bar{b}$ with $j_1 j_2 b\bar{b}$ mimicking the two jets in W decay and the two forward jets. The Feynman diagrams of the top-quark background are shown in Fig. 9.

We shall take the following kinematic cuts, reflecting the properties of the signal, to suppress the backgrounds and keep the signal as much as possible.

Cut 1: Requiring an isolated lepton $\ell^+(\mu^+, e^+)$ in the central rapidity region

$$N(\ell^+) = 1, \qquad N(\ell^-) = 0 \quad \text{with} \quad |\eta_{\ell^+}| < 2. \tag{43}$$

Since the signal lepton has larger probability of being in the central rapidity region than the RBs do, this cut will suppress the RBs relative to the signal. Furthermore, there can be fake leptons (ℓ^+ or ℓ^-) coming from the decays of the hadrons $\pi, \eta, J/\psi$, etc. in the hadronized jets. This cut can also suppress the fake leptons.

Cut 2: p_T(leptons)-cut

Let $\boldsymbol{p}_T(\ell^+)$ and $\not{\boldsymbol{p}}_T \equiv \boldsymbol{p}_T(\nu_\ell)$ be the transverse momentum vectors of ℓ^+ and ν_ℓ, respectively. Our simulation shows that a cut on $p_T(\text{leptons}) \equiv |\boldsymbol{p}_T(\ell^+) + \not{\boldsymbol{p}}_T|$ can effectively suppress both the IB and the RBs. Figure 10 plots the inclusive p_T(leptons) distributions of the signal plus IB (red-solid), the IB (pink-dotted), and the total RBs (blue-small-dotted) for example 500II with $\mathsf{L}_{\text{int}} = 100\ \text{fb}^{-1}$. We see from Fig. 10 that taking a cut

$$p_T(\text{leptons}) > 150\ \text{GeV} \tag{44}$$

can suppress both the IB and the total RBs, while keep the signal as much as possible. It can also suppress fake leptons very effectively since the scale of the transverse momenta of fake leptons is of the order of the hadronization scale which is much smaller than the required p_T(leptons) in (44).

Cut 3: Forward-jet cuts

The signal has two clear forward jets j_1^f and j_2^f which characterize the weak-boson fusion process, while in some RBs, the jets which mimic j_1^f and j_2^f may not be forward. So

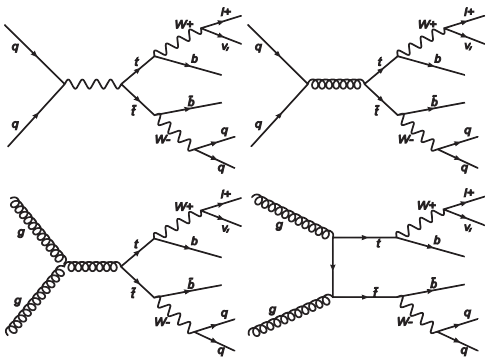

FIG. 9. Feynman diagrams for the top-quark backgrounds.

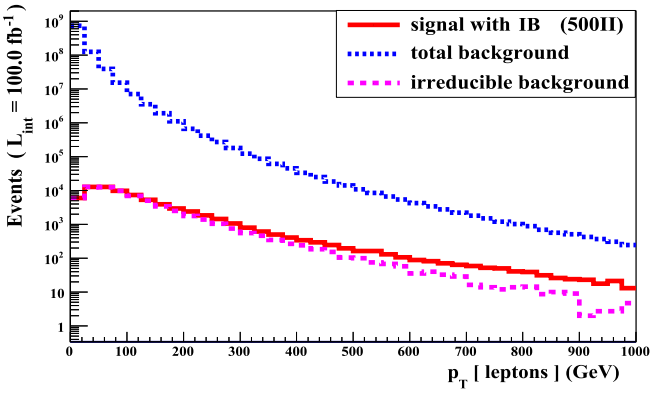

FIG. 10 (color online). p_T(leptons) distributions of signal + IB (red-solid), IB (pink-dotted), and total RBs (blue-small-dotted) in weak-boson scattering for example 500II with $\mathsf{L}_{\rm int} = 100$ fb^{-1}.

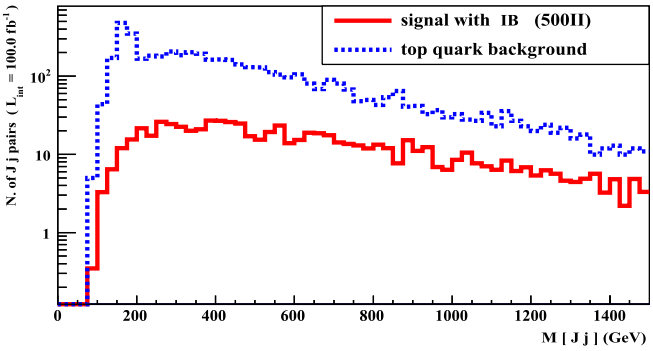

FIG. 11 (color online). $M(J, j)$ distributions of signal + IB (red-solid) and the top-quark background (blue-dotted) in weak-boson scattering for example 500II with $\mathsf{L}_{\rm int} = 100$ fb^{-1}.

that we can set cuts reflecting the properties of j_1^f and j_2^f to suppress the RBs. There have been several ways of setting the forward-jet cuts. We follow the way in Ref. [40] but with a little modification

$$\begin{aligned} &p_T(j^f) > 35 \text{ GeV}, \\ &E(j^f) > 300 \text{ GeV}, \\ &2.0 < |\eta(j^f)| < 5, \qquad \eta(j_1^f)\eta(j_2^f) < 0. \end{aligned} \tag{45}$$

In the cut for $|\eta(j^f)|$, we have taken account of the acceptance of the detector (cf. Table II). Here, instead of taking $p_T(j^f) > 20$ GeV as in Ref. [40], we take $p_T(j^f) > 35$ GeV for avoiding the pileup events.

In our simulation, we take the jet with the most positive η and the jet with the most negative η to satisfy the rapidity requirement in (45).

Cut 4: Fat jet cuts

In the signal, the fat jet J (the jet with largest transverse momentum) is the decay product of a W boson, so that the invariant mass $M(J)$ of J should equal to M_W. Considering the resolution of the detector, we set the requirement

$$70 \text{ GeV} < M(J) < 100 \text{ GeV}. \tag{46}$$

This requirement can effectively suppress the largest reducible background $W + 3j$ since, in $W + 3j$, the largest p_T ordinary jet $\hat{j}$ which mimics J comes from the clustering of the parton showers from a massless parton. For most of the probability, its mass $M(\hat{j})$ is much smaller than the requirement (46).

Furthermore, in the signal, the fat jet J and the isolate lepton ℓ^+ are decay products of the two W bosons in H decay. With the cut (43), we also set

$$|\eta_J| < 2 \tag{47}$$

to suppress the backgrounds.

Cut 5: Top-quark veto

We see from Fig. 9 that, in a top-quark background event, $t \to W^+ b \to \ell^+ \bar{\nu}_\ell b$, $\bar{t} \to W^- \bar{b} \to J\bar{b}$. So that, to identify a top-quark background event, we can construct the invariant mass $M(J, \bar{b})$ to reconstruct the top quark. Experimentally, $M(J, \bar{b})$ must be in the top-quark resonance region around m_t. On the other hand, if we construct $M(J, b)$ it will not be in the top-quark resonance region. However, in the experiment, we can just see three jets J, j_1, j_2 in the final state, and cannot identify which one of j_1 and j_2 is the $\bar{b}$ jet. So we should construct two invariant masses $M(J, j_1)$ and $M(J, j_2)$ to see if one of them is in the top-quark resonance region to identify whether an event is a top-quark background event. In Fig. 11 we plot the $M(J, j_1)$ [or $M(J, j_2)$]

TABLE III. Cut efficiencies expressed in terms of the tree-level cross sections σ_{S+IB} and σ_B (in unit of fb) in the weak-boson scattering process. The first five columns are values of σ_{S+IB} for the five examples, and the last four columns are values σ_B for four kinds of backgrounds.

	σ_{S+IB}					σ_B			
	400II	500I	500II	800I	800II	IB	W + jets	$t\bar{t}$	WV + jets
Without cuts	2085	2037	2009	1917	1996	1925	31500000	92000	7600
Cut 1	759	740	726	679	705	669	9360000	35792	2506
Cut 2	210	209	185	149	162	138	44270	5298	499
Cut 3	11.5	11.0	14.6	10.6	11.3	8.51	370	123	13.7
Cut 4	1.20	1.28	2.33	1.59	1.92	0.682	5.47	10.3	1.53
Cut 5	0.936	0.921	1.80	1.22	1.56	0.474	3.49	2.04	0.81

distribution from our simulation including the signal plus IB (red-solid) and the top-quark background (blue-dotted) distributions for example 500II with $\mathsf{L}_{\rm int} = 100$ fb^{-1}. We see that the top-quark resonance region is between 130 and 240 GeV [40]. So if, in an event, one of the invariant masses $M(J, j_1)$ and $M(J, j_2)$ is in the region

$$130 \text{ GeV} < M(J, j) < 240 \text{ GeV}, \tag{48}$$

we should veto the event. Equivalently, we only take the events in which both $M(J, j_1)$ and $M(J, j_2)$ are outside the region (48). In this way, we can effectively veto the top-quark background events.

Actually, there are more untagged jets apart from the tagged jets J, j_1, and j_2 in the result of the anti-k_T algorithm. For safety, we have also checked the constraint (48) for invariant masses of J with all other untagged jets.

To see the efficiency of each cut, we list the values of the cross sections [in fb] for signal plus IB (for the five examples mentioned in Sec. I) and various backgrounds after each cut in Table III. We see that, with all these cuts, the backgrounds can be effectively suppressed.

We see that, before imposing the cuts, the $W+$jets background is larger than the signal plus IB by a factor of 1.5×10^4. After Cut 1–Cut 5, it is reduced to the same order of magnitude as the signal plus IB.

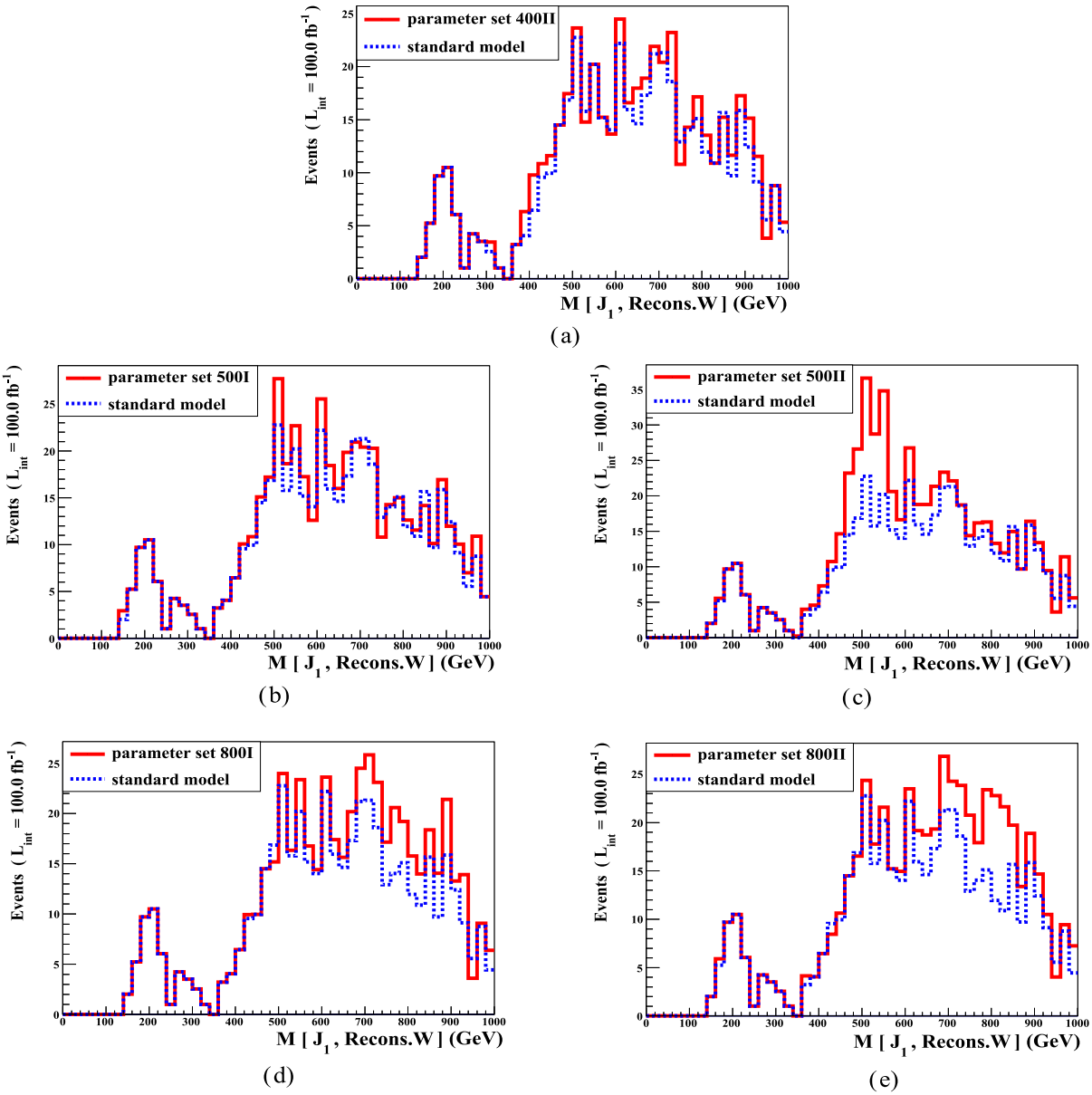

FIG. 12 (color online). Invariant mass $M(J_1, \text{recons } W)$ distributions (red-solid) for the five examples [(a) 400II, (b) 500I, (c) 500II, (d) 800I, and (e) 800II], together with that of the SM (blue-dotted) for comparison, with $\mathsf{L}_{\rm int} = 100$ fb^{-1}.

TABLE IV. Required integrated luminosity L_{int} (in unit of fb^{-1}) for the statistical significance of $1\sigma, 3\sigma$, and 5σ for the five examples in weak-boson scattering.

	$L_{int}[fb^{-1}]$				
	400II	500I	500II	800I	800II
1σ	32	34	3.9	12	5.7
3σ	288	397	35	110	52
5σ	800	852	96	306	143

Now the cross sections are of the order of 1 fb, so that for an integrated luminosity of 50–100 fb^{-1}, there can be several tens to hundreds of events which are detectable in the first few years run of the 14 TeV LHC.

From Eqs. (40)–(42), we obtain the following required integrated luminosity for the statistical significance of 1σ, 3σ, and 5σ for the five examples mentioned in Sec. I (cf. Table IV).

We see that examples 500II and 800II hope to be discovered (at the 5σ level) in the first few years run of the 14 TeV LHC, while 800I can be discovered (at the 5σ level), and 400I and 500I can have evidence (at the 3σ level) for an integrated luminosity of 300 fb^{-1} at the 14 TeV LHC.

Of course we have only taken account of the statistical error here, and we leave the study of the systematic errors to the experimentalists.

There is a missing neutrino in the final state. We take the method of determining the neutrino longitudinal momentum from the requirement of reconstructing the correct value of the W boson mass suggested by Ref. [40]. There are two solutions of the longitudinal momentum of the neutrino. We take the solution with smaller p_z as is conventionally used [45,46]. Then we can calculate the invariant mass of the fat jet and the reconstructed W boson.

In Fig. 12, we plot the invariant mass $M(J_1, \text{recons } W)$ distributions (red-solid) for five examples, together with that of the SM distribution (blue-dotted) for comparison, with an integrated luminosity of 100 fb^{-1}.

We see that there are excess events over the SM results around M_H. This can be a signal of the contribution of the intermediate state heavy Higgs boson. So an observation of the excess events can be a way of discovering the heavy Higgs boson. Comparing the five distributions in Fig. 12, we see that the excess events are more significant for heavier H than for lighter H.

VII. PROBING HEAVY NEUTRAL HIGGS BOSONS VIA $pp \to VH^* \to VVV$ ASSOCIATED PRODUCTION

Now we study the process $pp \to VH^* \to VVV \to \ell^+\nu_\ell j_1 j_2 j_3 j_4$, $V = W, Z$. Here the W boson decaying to $\ell^+\nu_\ell$ can be either the weak boson associated with H or a weak boson in H decay. The other two weak bosons decay to $j_1 j_2 j_3 j_4 \sim J_1 J_2$, where J_1 and J_2 are two fat jets. From now on, we take a convention regarding J_1 as the fat jet with the largest transverse momentum, and J_2 as the one with the second largest transverse momentum.

The Feynman diagrams for the signal and example of the IB are shown in Fig. 13.

Again, these two amplitudes have interference, so that they should be calculated together.

Next we consider the RBs. Now the largest QCD background is the inclusive $W + 2j$ when $W \to \ell^+\nu_\ell$ and the two

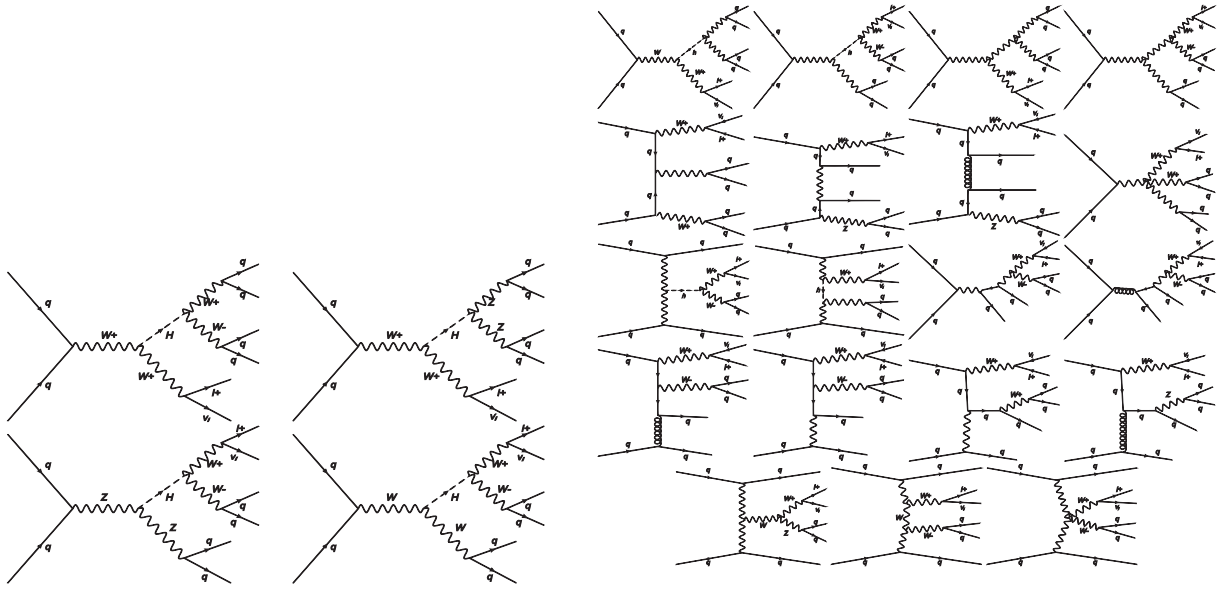

(a) (b)

FIG. 13. Feynman diagrams in VH associated production. (a) The signal, (b) examples of the IB.

jets mimic the two fat jets in the signal. For safety, we take into account all the $W+$ jets and the $W+V+$ jets processes to do the simulation, and pick up the parts that can mimic the signal as the QCD backgrounds. For the top-quark background, we make the same treatment (cf. Fig. 9).

We then make the following kinematic cuts for suppressing the backgrounds.

Cut 1: Leptonic cuts

Similar to what we did in Sec. II, we require an isolated ℓ^+ (μ^+, e^+) in the detectable rapidity region (cf. Table II), i.e.,

$$N(\ell^+) = 1, \qquad N(\ell^-) = 0 \quad \text{with} \quad \eta_{\ell^+} < 2.4. \tag{49}$$

Next we make the cut on $p_T(\text{leptons})$. The inclusive $p_T(\text{leptons})$ distributions of the signal plus IB, the RB, and the total background are shown in Fig. 14. Here, we do not have to take care of the transverse momentum balance with the forward jets as in Sec. II, so we can take a stronger cut

$$|p_T(\text{leptons})| > 400 \text{ GeV} \tag{50}$$

to suppress more backgrounds. This cut can also strongly suppress the fake leptons.

Cut 2: Fat jet cuts

As mentioned in Sec. II, we require the first two large transverse momenta to satisfy

$$\begin{aligned} 70 \text{ GeV} < M(J_1) < 100 \text{ GeV} \\ 70 \text{ GeV} < M(J_2) < 100 \text{ GeV}. \end{aligned} \tag{51}$$

This can suppress the backgrounds with ordinary jets.

Cut 3: Top-quark veto

As in Sec. II, for suppressing the top-quark background, we construct two invariant masses $M(J, j_1)$ and $M(J, j_2)$, where $J = J_1$ or J_2, and j_1, j_2 are the two observed jets from the partons b or $\bar{b}$ in Fig. 9. In Fig. 15 we plot the

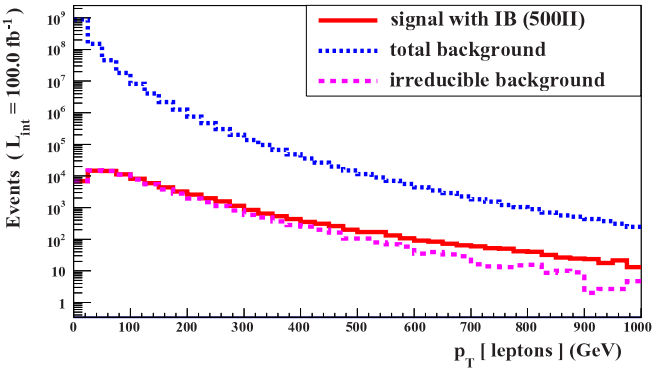

FIG. 14 (color online). $p_T(\text{leptons})$ distributions of signal + IB (red-solid), IB (pink-dotted), and total RBs (blue-small-dotted) in the $pp \to VH^* \to VVV$ process for example 500II with $\mathsf{L}_{\text{int}} = 100$ fb^{-1}.

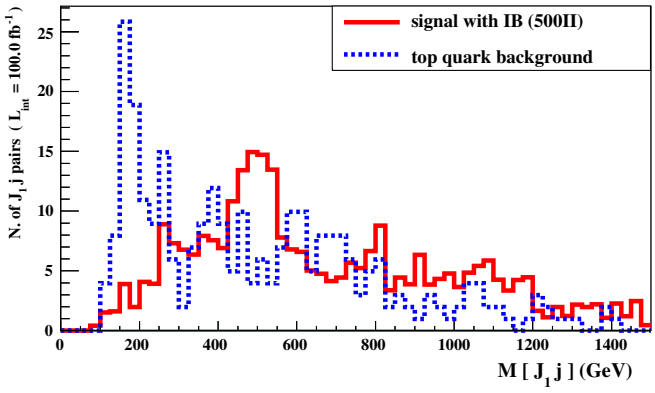

FIG. 15 (color online). $M(J, j)$ distributions of signal + IB (red-solid) and the top-quark background (blue-dotted) in the $pp \to VH^* \to VVV$ process for example 500II with $\mathsf{L}_{\text{int}} = 100$ fb^{-1}.

$M(J, j_1)$ [or $M(J, j_2)$] distribution from our simulation including the signal plus IB (red-solid) and the top-quark background (blue-dotted) distributions for example 500II with $\mathsf{L}_{\text{int}} = 100$ fb^{-1}. We can see clearly the top-quark peak (in the blue-dotted curve) in the region 130 GeV $< M(J, j) <$ 240 GeV for $j = j_1$ or j_2.

As in Sec. II, we set the cut

$$130 \text{ GeV} < M(J, j) < 240 \text{ GeV}, \tag{52}$$

to suppress the top-quark background. We should veto the event if one of $M(J, j_1)$ and $M(J, j_2)$ satisfies (52). Equivalently, we only take the events in which both $M(J, j_1)$ and $M(J, j_2)$ are outside the region (52). In this way, we can effectively veto the top-quark background events.

Cut 4: The $\Delta R(\ell^+, J_1,)$ cut

In VH associated production, because H is heavy and has a quite large momentum, the recoil transverse momentum of the associated V boson is generally large. Furthermore, due to the large momentum of the heavy Higgs boson H, the angular distance between two weak

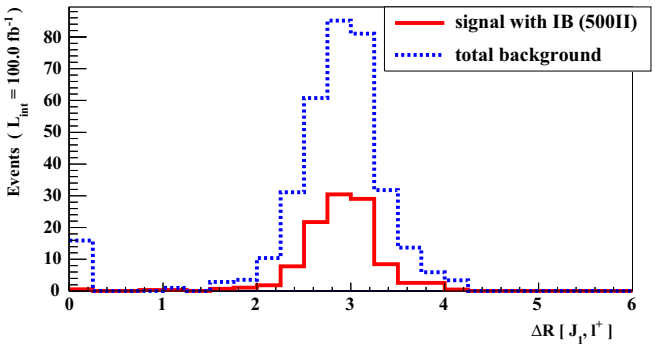

FIG. 16 (color online). $\Delta R(\ell^+, J_1)$ distributions of signal + IB (red-solid) and the total background (blue-dotted) in the $pp \to VH^* \to VVV$ process for example 500II with $\mathsf{L}_{\text{int}} = 100$ fb^{-1}.

TABLE V. Cut efficiencies expressed in terms of the tree-level cross sections σ_{S+IB} and σ_B (in units of fb) in the $pp \to VH^* \to VVV$ process. The first five columns are values of σ_{S+IB} for the five examples, and the last four columns are values σ_B for four kinds of backgrounds.

	σ_{S+IB}					σ_B			
	400II	500I	500II	800I	800II	IB	W + jets	$t\bar{t}$	WV + jets
Without cuts	2085	2037	2009	1917	1996	1925	31500000	92000	7600
Cut 1	46.9	54.4	25.7	18.6	25.3	13.1	1422	65.9	47.9
Cut 2	2.78	4.36	1.21	0.629	1.41	0.211	2.91	0.716	0.336
Cut 3	2.32	3.79	1.08	0.526	1.24	0.13	2.15	0.149	0.25
Cut 4	2.04	3.21	0.921	0.426	1.11	0.061	1.39	0.060	0.179

bosons from H decay is small, while that between the weak boson associated with H and any of the weak bosons in H decay is large. If ℓ^+ comes from the W boson associated with H, the angular distance between ℓ^+ and any of the fat jets is large. If ℓ^+ comes from the decay of H, there must be a fat jet J_1 (actually from the V boson associated with H) with large $\Delta R(\ell^+, J_1)$. The background does not have this situation. We plot, in Fig. 16, the $\Delta R(\ell^+, J_1)$ distributions of the signal plus IB (red-solid) and the total background (blue-dotted) in the VH associated production for example 500II with $\mathsf{L}_{\rm int} = 100$ fb^{-1}. We see that the main distribution of the red-solid curve is indeed located further right to that of the blue-dotted curve. So that a cut

$$\Delta R(\ell^+, J_1) > 2.5 \tag{53}$$

can suppress the total background.

We know that Cut 1 on the leptons can effectively avoid the fake leptons from ordinary jets to mimic the signal lepton. However, since the fat jets J_1 and J_2 have quite large transverse momenta, Cut 1 may not be sufficient to suppress the fake leptons from the fat jets. Therefore, we should require the lepton not to overlap with any of the fat jets. Since we have taken $R = 0.7$ in jet formations, this means both $\Delta R(\ell^+, J_1)$ and $\Delta R(\ell^+, J_2)$ should be larger than 0.7. Cut 4 already guarantees $\Delta R(\ell^+, J_1)$ to satisfy this requirement. So we add the requirement

$$\Delta R(\ell^+, J_2) > 0.7 \tag{54}$$

here.

To see the efficiency of each cut, we list the values of the cross sections (in fb_ for signal plus IB (for the five examples mentioned in Sec. I) and various backgrounds after each cut in Table V. We see that, with all these cuts, the backgrounds can be effectively suppressed. Compared with the numbers in Table III, we see that all the backgrounds in Table V are more suppressed. Again, the signal plus IB cross section is of the order of 0.4–3 fb, so that for an integrated luminosity of around 100 fb^{-1}, we can have a few tens to a few hundreds of events.

From Eqs. (40)–(42), we obtain the required integrated luminosity for the statistical significance of 1σ, 3σ, and 5σ for the five examples mentioned in Sec. I (cf. Table VI).

TABLE VI. Required integrated luminosity $\mathsf{L}_{\rm int}$ (in units of fb^{-1}) for the statistical significance of $1\sigma, 3\sigma$, and 5σ for the five examples in the $pp \to VH^* \to VVV$ process.

	$\mathsf{L}_{\rm int}$[fb^{-1}]				
	400II	500I	500II	800I	800II
1σ	0.43	0.18	2.3	13	1.6
3σ	3.9	1.6	21	115	14
5σ	10.8	4.5	57	319	39

We see that, except for 800I, all the other four examples hope to be discovered (5σ) in the first few years run of the 14 TeV LHC, while 800I can have evidence (3σ) for $\mathsf{L}_{\rm int} = 115$ fb^{-1}, and can be discovered (5σ) for $\mathsf{L}_{\rm int} = 319$ fb^{-1} at the 14 TeV LHC. These are conclusions considering only the statistical errors.

Finally, we deal with the issue of experimentally discovering H and measuring M_H. In addition to Cut 4, we add a cut

$$\Delta R(\ell^+, J_2) > 2.5, \tag{55}$$

where J_2 is the other fat jet. Then both J_1 and J_2 will mainly come from the decay of H, and thus the invariant mass $M(J_1, J_2)$ will show the H peak at $M(J_1, J_2) = M_H$. Since the uncertainties in identifying the fat jet from a boosted W boson decay are small [41], measuring the $M(J_1, J_2)$ distribution is quite feasible experimentally.

Figure 17 shows the $M(J_1, J_2)$ distributions for examples 400II, 500I, 500II, and 800II. We see that sharp peaks can be seen clearly, and thus the heavy Higgs boson and its mass can be detected experimentally. This is the advantage of the $pp \to VH^* \to VVV$ process.

The example 800I is special. It has a very large decay width due to the largeness of $\Gamma(H \to t\bar{t})$, so that there cannot be a sharp peak showing up. However, due to the fact that $M_H \gg M_h$ in this example, the heavy Higgs boson H moves much more slowly than the light Higgs boson h does. Therefore, $\Delta R(\ell^+, J_2)$ for H is larger than that for h in the SM background. In Fig. 18 we plot the $\Delta R(\ell^+, J_2)$ distributions of the signal plus IB (red-dotted) and the SM

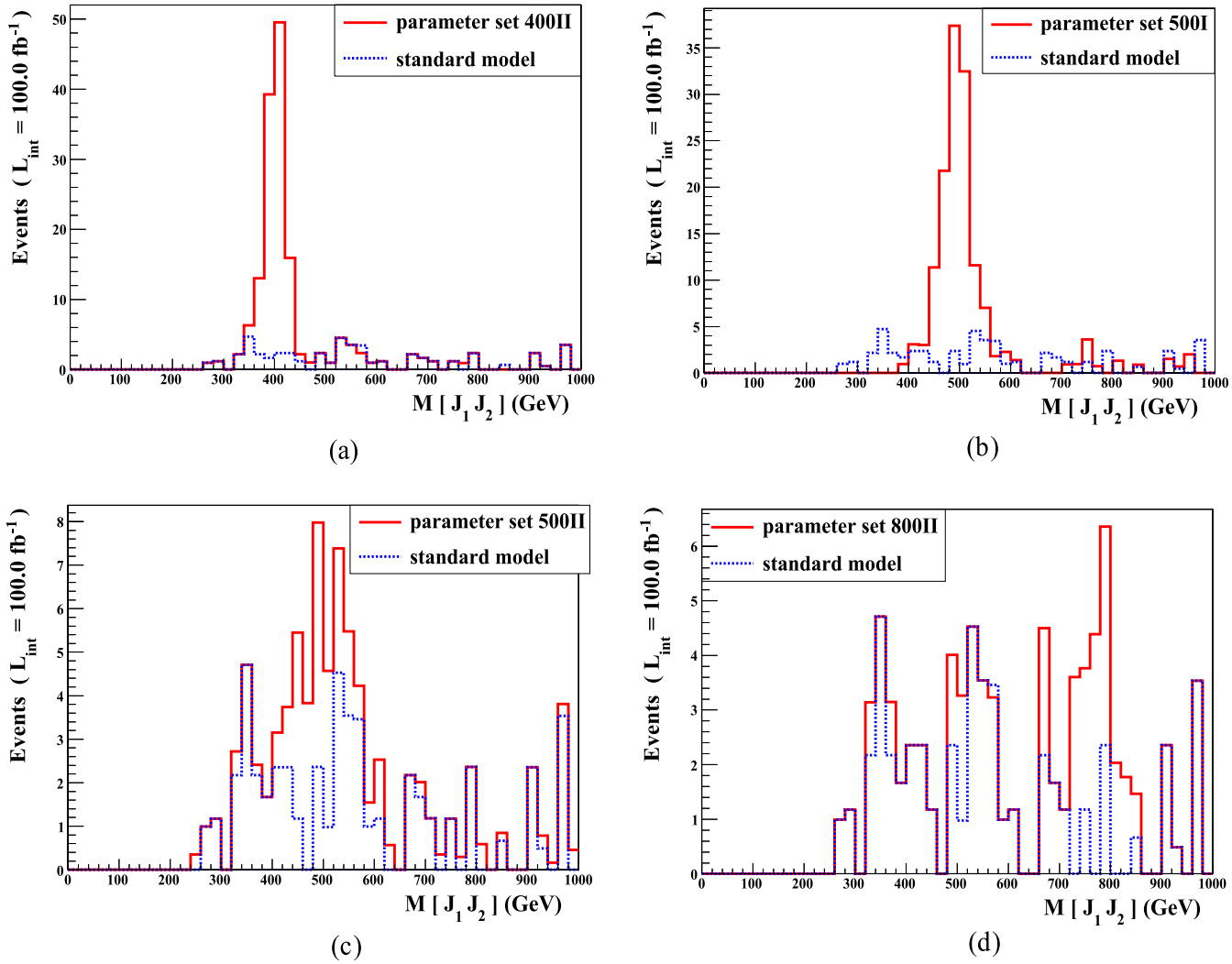

FIG. 17 (color online). Invariant masses $M(J_1, J_2)$ in the $pp \to VH^* \to VVV$ process after all cuts and $\Delta R(\ell^+, J_2) > 2, 5$ for the following examples: (a) 400II, (b) 500I, (c) 500II, and (d) 800II.

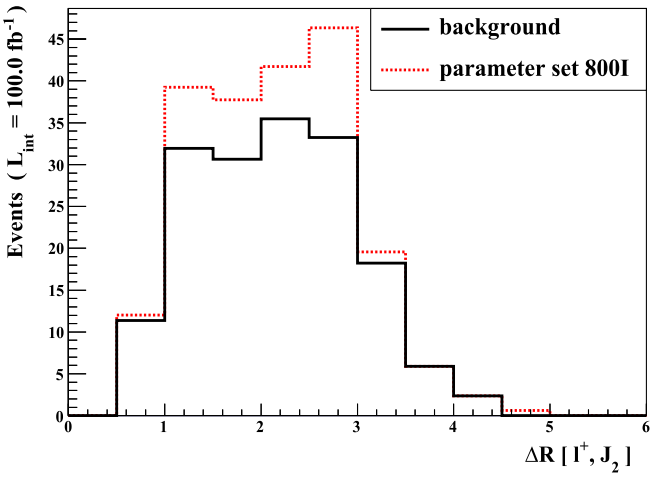

FIG. 18 (color online). $\Delta R(\ell^+, J_2)$ distributions of signal + IB (red-dotted) and the total background (dark-solid) in the $pp \to VH^* \to VVV$ process for example 800I with $\mathsf{L}_{\text{int}} = 100$ fb^{-1}.

background (dark-solid) in the range $\Delta R(\ell^+, J_2) > 0.7$ due to (54).

We see that the main distribution of the signal plus IB is located around $\Delta R(\ell^+, J_2) = 2.7$ which is right to that of the SM background at around $\Delta R(\ell^+, J_2) = 2.3$, and the height of the signal plus IB is higher. This can be seen as a characteristic feature of the heavy Higgs boson contribution in example 800I.

In principle, we can replace the cut (55) by $\Delta R(J_1, J_2) > 2.5$ to extract the contribution of the Feynman diagram in which the leptons are from the H decay, and use the reconstruction method suggested in Ref. [40] to calculate the invariant mass $M(J_1, \text{recons } W)$ distribution as we did in Fig. 12. However, our result shows that the obtained resonance peaks are less clear than those in Fig. 17. So we only suggest the method presented above.

From Fig. 17 we see that the excess of events over the SM result is more significant for the lighter Higgs boson

than for the heavier Higgs boson. This is just the opposite to that in the VV scattering process (cf. the last paragraph in Sec. II). This means that the VV scattering process and the $pp \to VH^* \to VVV$ process are complementary to each other in this respect.

Having found the resonance, the next task is to determine whether its spin is really zero. This can be done by studying the decay mode $H \to ZZ \to 4\ell$ [47] which needs a much larger integrated luminosity. Another possible way is to measure the azimuthal angle dependence as suggested by Ref. [48].

VIII. MEASURING THE ANOMALOUS COUPLING CONSTANTS f_w AND f_{ww}

If we can measure the values of the anomalous coupling constants f_W and f_{WW} which characterize the heavy neutral Higgs boson H, it will be a new high energy measurement of the property of the nature, and will serve as a new high energy criterion for the correct new physics model. All new physics models predicting f_W and f_{WW} not consistent with the measured values should be ruled out. The necessary condition for surviving new physics models is that their predicted f_W and f_{WW} should be consistent with the measured values. We shall see that this measurement is really possible.

It has been pointed out in Ref. [33] that, for a single-Higgs system, measuring both the cross section and the leptonic transverse momentum distribution in weak-boson scattering processes may determine the values of f_W and f_{WW} to a certain precision. However, in our present case with both h and H contributions, the weak-boson scattering process is not so optimistic for this purpose. So we concentrate on studying the measurement of f_W and f_{WW} in the $pp \to VH^* \to VVV$ process.

A. The case of $M_H = 500$ GeV as an example

Let us take the case of $M_H = 500$ GeV as an example. After measuring the resonance peak experimentally, we can impose an additional cut

$$400 \text{ GeV} < M(J_1, J_2) < 600 \text{ GeV} \tag{56}$$

to take the events in the vicinity of the resonance peak to further improve the signal to background ratio. Now we take four sets of the anomalous coupling constants f_W and f_{WW}, and see if there can be certain new observables to distinguish them. We take

set I: $C_t = 1$, $\rho_h = 0.8$, $\rho_H = 0$, and $f_W = f_{WW} = 0$ (background).

set II: $C_t = 0.6$, $\rho_h = 0.8$, $\rho_H = 0.6$ and $f_W = -f_{WW} = 6$ TeV^{-2}.

set III: $C_t = 0.6$, $\rho_h = 0.8$, $\rho_H = 0.6$, and $f_W = 12$ fb$^{-2} \gg f_{WW} = 0$.

set IV: $C_t = 0.6$, $\rho_h = 0.8$, $\rho_H = 0.6$, and $f_W = 0 \ll f_{WW} = 12$ fb^{-2}.

We can now construct several observables which may be able to distinguish the four sets of f_W and f_{WW} listed above, namely, (a) the $p_T(\text{leptons})$ distribution, (b) the $p_T(J_1)$ distribution, (c) the $\Delta R(\ell^+, J_2)$ distribution, and (d) the $\Delta R(J_1, J_2)$ distribution. In the two transverse momentum distributions, the additional cuts (56) and $\Delta R(\ell^+, J_2) > 2.5$ are taken, while in the two angular distance distributions none of these additional cuts are taken.

In Fig. 19 we plot these four distributions for the four sets of f_W and f_{WW} with $\mathsf{L}_{\text{int}} = 100$ fb^{-1}, where the dark-solid, red-dotted, pink-dashed, and blue-dashed-dotted curves stand for set I, set II, set III and set IV, respectively.

We see that, in all the four distributions, the curves of the four sets can be clearly distinguished. The differences between different sets in Fig. 19(c) and Fig. 19(d) are more significant. Therefore, measuring the four distributions experimentally, and checking with each other, the relative size of f_W and f_{WW} existing in the nature can be obtained, and together with the measurement of the cross section, the values of f_W and f_{WW} can be separately determined, which gives the new criterion for discriminating new physics models. This is an important advantage of the $pp \to VH^* \to VVV$ process.

B. The case of $M_H = 800$ GeV as an example

Since in the case of 800I no clear peak can be seen and it can only be realized by the distribution in Fig. 18, we now examine whether it is possible to measure the values of f_W and f_{WW} in this case. In Fig. 20 we plot the $p_T(J_1)$ and $\Delta R(J_1, J_2)$ distributions for the $M_H = 800$ GeV case with four sets of parameters as those in the case of $M_H = 500$ GeV but with $C_t = 1$. We see that the four sets of f_W and f_{WW} can all be clearly distinguished.

IX. SUMMARY AND DISCUSSION

To search for new physics beyond the SM, we suggest searching for heavy neutral Higgs bosons which are generally contained in new physics models.

We summarize our results as follows.

(i) In this paper, we have considered an arbitrary new physics theory containing more than one Higgs boson $\Phi_1, \Phi_2, \ldots$ taking account of their mixing effect. For generality, we do not specify the EW gauge group except requiring that it contains an $SU(2)_L \times U(1)$ subgroup with the gauge bosons W, Z, and γ. We also neither specify the number of $\Phi_1, \Phi_2, \ldots$, nor specify how they mix to form mass eigenstates except to identify the lightest Higgs boson h to the recently discovered $M_h = 125$–126 GeV Higgs boson. Then we study the general properties of the couplings of both the lightest Higgs boson h and a heavier neutral Higgs boson H (lighter than other heavy Higgs

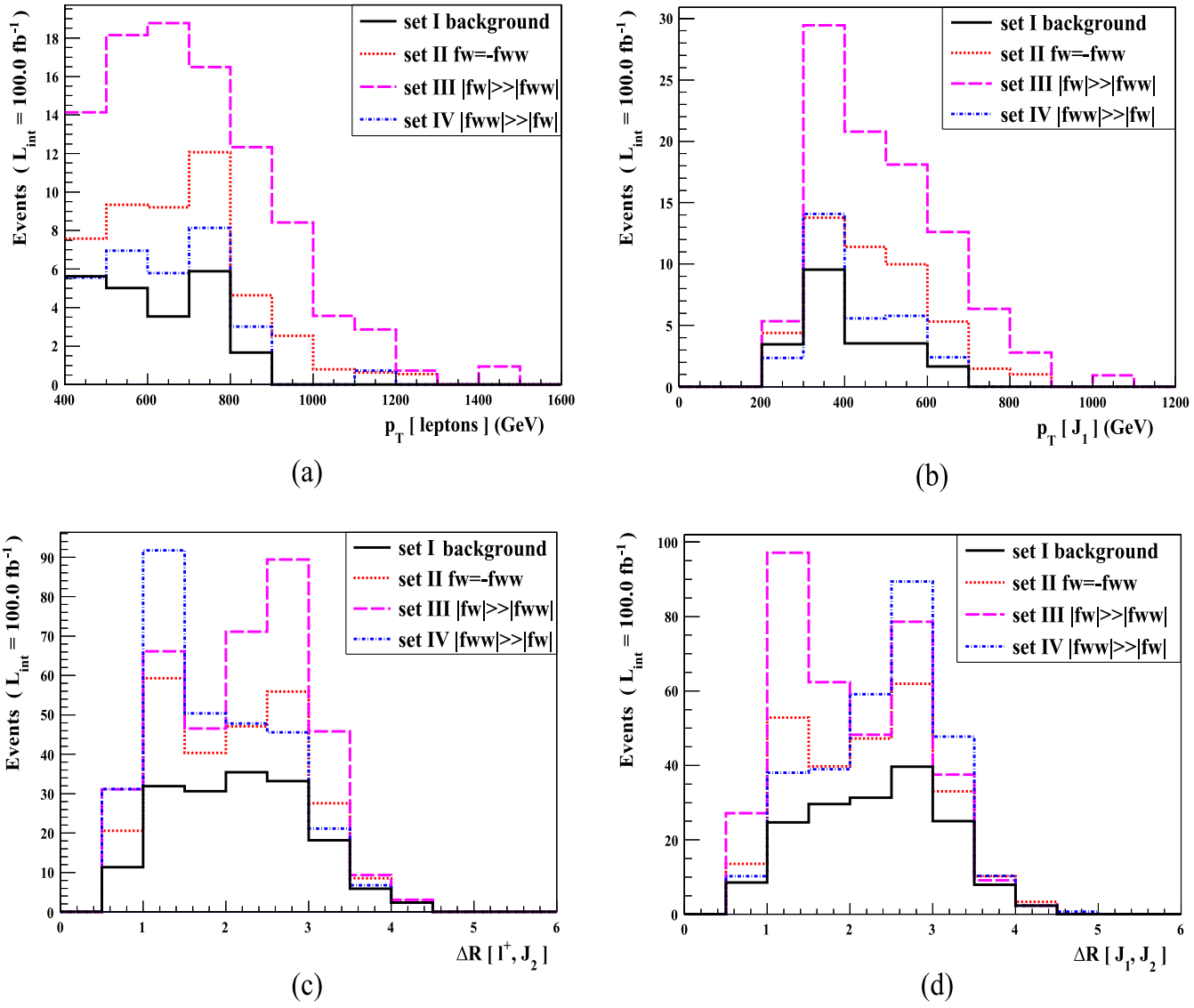

FIG. 19 (color online). (a) The p_T(leptons) distribution [with (56) and $\Delta R(\ell^+, J_2) > 2.5$], (b) the $p_T(J_1)$ distribution [with (56) and $\Delta R(\ell^+, J_2) > 2.5$], (c) the $\Delta R(\ell^+, J_2)$ distribution [without (56) and $\Delta R(\ell^+, J_2) > 2.5$], and (d) the $\Delta R(J_1, J_2)$ distribution [without (56) and $\Delta R(\ell^+, J_2) > 2.5$], with $\mathsf{L}_{\rm int} = 100$ fb^{-1}. The dark-solid, red-dotted, pink-dashed, and blue-dashed-dotted curves stand for set I, set II, set III and set IV, respectively.

bosons). The probe of gauge-phobic heavy neutral Higgs bosons are not considered in this study, and will be studied elsewhere.

We first gave a general model-independent formulation of the couplings of h and H to fermions and gauge bosons based on the idea of the effective Lagrangian up to dim-6 operators in Sec. II. The obtained effective couplings for the Higgs-gauge interaction are different from the traditional ones constructed for a single-Higgs system by containing new parameters ρ_h and ρ_H reflecting the Higgs mixing effect. After taking account of the constraints from the known low energy experiments, there are seven unknown coupling constants left, namely, the gauge coupling constant ρ_h in the dim-4 gauge interaction of h [cf. Eq. (5)], the gauge coupling constant ρ_H in the dim-4 gauge interaction of H [cf. Eq. (6)], the anomalous coupling constants f_W, f_{WW}, f_B, f_{BB} in the dim-6 gauge interactions of H [cf. (10) and (11)], and the anomalous Yukawa coupling constant C_t of H [cf. Eq. (2)], and the corresponding momentum representations are given in Eqs. (13), (14), (15), (16), (17), and (18).

(ii) To estimate the possible range of the anomalous coupling constants f_W, f_{WW}, f_B, f_{BB}, we first studied the theoretical constraints from the requirement of the unitarity of the S matrix of weak-boson scattering in Sec. III. We took the effective W approximation to calculate the scattering amplitudes, and calculated the constraints on f_W and f_{WW} by a two-parameter

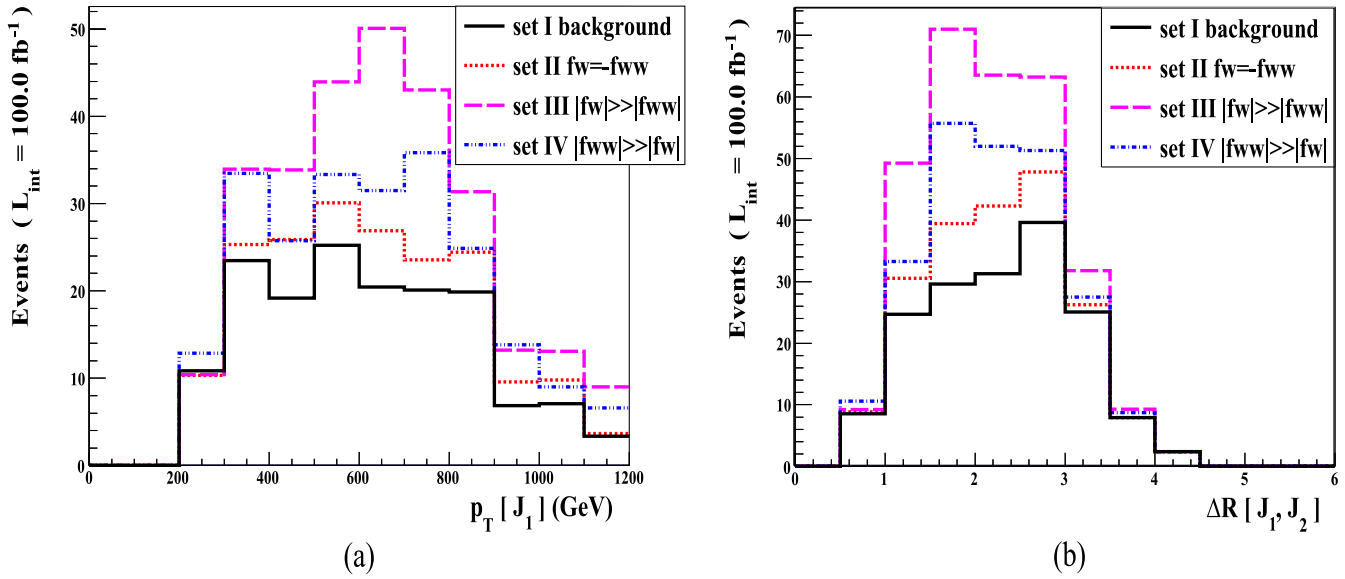

FIG. 20 (color online). (a) The $p_T(J_1)$ distribution and (b) the $\Delta R(J_1, J_2)$ distribution for $M_H = 800$ GeV with $\mathsf{L}_{\text{int}} = 100$ fb^{-1}. The meaning of the curves is the same as in Fig. 19 but with $C_t = 1$.

numerical analysis. The obtained constraints are shown in Fig. 2.

(iii) We further studied the experimental constraints from the ATLAS and CMS experiments in Sec. IV to obtain further constraints. Anomalous coupling constants consistent with both the unitarity constraints and the experimental constraints are the available anomalous couplings that an existing heavy neutral Higgs boson can have.

We first make an approximation of neglecting the anomalous coupling constants in the $H\gamma\gamma$ and $HZ\gamma$ couplings inspired by the trend of the ATLAS and CMS measurements of $\mu = \sigma/\sigma_{\text{SM}}|_{95\%\text{ C.L.}}$ in the decay channels $H \to \gamma\gamma$ and $H \to Z\gamma$. This approximation leads to the constraints (32) and (33) which simplifies our analysis.

Then we consider the CMS exclusion bounds on the SM Higgs boson for the Higgs mass up to 1 TeV, to obtain the experimental bounds on f_W and f_{WW}. The calculation is to full leading order in perturbation. We took the cases of 400II, 500I, and 500II as examples. In our calculation of the total decay width of H, we have made a conservative approximation. The obtained conservative experimental constraints and the *available* regions of f_W and f_{WW} are shown as the blue shaded regions in Figs. 3, 4, and 5. This guarantees that a heavy Higgs boson H, with its f_W and f_{WW} in the blue shaded regions, is definitely not excluded by the CMS exclusion bound [10]. In the cases of 800I and 800II, there is almost no experimental constraint on f_W and f_{WW} because the CMS exclusion bound is very loose at $M_H = 800$ GeV.

(iv) In this paper, for studying the LHC signatures of H, we suggest taking VV scattering and $pp \to VH^* \to VVV$ as sensitive processes for probing the anomalous heavy Higgs boson model independently at the 14 TeV LHC. We take the general model-independent formulation of the heavy Higgs couplings in Sec. II. and take five sets of anomalous coupling constants allowed by the unitarity constraint and the present CMS experimental exclusion bound as examples to do numerical simulation, namely, 400II, 500I, 500II, 800I, 800II with the heavy Higgs mass $M_H = 400$, 500, and 800 GeV (cf. Sec. IV). The calculations are to the hadron level. We take the CTEQ6.1 parton distribution functions [34], and use MADGRAPH5 [27] to do the full tree-level simulation. The parton shower and hadronization are calculated with PYTHIA6.4 [35], and the anti-k_T algorithm with $R = 0.7$ [36] in DELPHES 3 [32] is used for the formation of jets. We also use DELPHES 3 to simulate the detecting efficiency of the detector.

(v) We first study the semileptonic decay mode of weak-boson scattering, i.e., $pp \to VVj_1^f j_2^f \to \ell^+\nu_\ell j_1 j_2 j_1^f j_2^f$. The Feynman diagrams of the signal and backgrounds are shown in Figs. 6–9. The largest background is the QCD background, the inclusive $pp \to W + 3j$ which is larger than the signal plus IB by 4 orders of magnitude. To suppress the backgrounds, we imposed five kinematic cuts given in Eqs. (43)–(48) which can effectively suppress the backgrounds. The cut efficiencies of each cut are listed in Table III, and the required integrated luminosities for 1σ deviation, 3σ evidence, and 5σ discovery are shown in Table IV. It shows that examples 500II and 800II hope to be discovered (at the 5σ level) in the first few years run of the 14 TeV LHC, while 800I can be discovered (at the 5σ level), and 400I and

500I can have evidence (at the 3σ level) for an integrated luminosity of 300 fb^{-1} at the 14 TeV LHC. We then took the method of determining the longitudinal momentum of the neutrino by requiring that the W boson mass be reconstructed correctly [40], and with which we calculated the invariant mass $M(J_1, \text{recons } W)$ distributions as shown in Fig. 12. We see that there are evident excesses of events over the SM result around $M(J_1, \text{recons } W) = M_H$. This can be the signal of the contribution of the intermediate state heavy Higgs boson. We also see that the excess of events are more significant for the heavier Higgs boson than for the lighter Higgs boson.

(vi) We then study the semileptonic mode of the $pp \to VH^* \to VVV$ process, $pp \to VH^* \to VVV \to \ell^+\nu_\ell j_1 j_2 j_3 j_4 \to \ell^+\nu_\ell J_1 J_2$ (J_1 and J_2 stand for the fat jets with largest and second largest transverse momenta, respectively). The Feynman diagrams for the signal and IB are shown in Fig. 13. Reducible backgrounds include the $W + 2$ jet, and the top-quark background similar to those in the weak-boson scattering process. We also imposed five kinematic cuts in Eqs. (49)–(54). The cut efficiencies after each cut are listed in Table V which shows that all backgrounds are more effectively suppressed. The required integrated luminosities for 1σ deviation, 3σ evidence, and 5σ discovery are shown in Table VI. Except for example 800I, all the other four examples hope to be discovered (5σ level) in the first few years run of the 14 TeV LHC, while 800I can have an evidence (3σ) for $\mathsf{L}_{\text{int}} = 115$ fb^{-1}, and can be discovered (5σ) for $\mathsf{L}_{\text{int}} = 319$ fb^{-1} at the 14 TeV LHC. In Fig. 17, we plot the invariant mass distributions $M(J_1, J_2)$ for examples 400II, 500I, 500I, and 800II, which shows that the resonance peaks for all these four examples are clearly seen. This makes it possible for the experimental search for the heavy Higgs boson H and the measurement of its mass M_H. For example 800I, due to the large decay rate of $\Gamma(H \to t\bar{t})$, the total decay width of H is very large such that there is no clear peak showing up. However, Fig. 18 shows a characteristic feature of the $M_H = 800$ GeV Higgs boson in the $\Delta R(\ell^+, J_2)$ distribution, which can help the experiment to find out the contribution of the heavy Higgs boson H. We see that the excess of events are more significant for the lighter Higgs boson than for the heavier Higgs boson. This is just the opposite to the case of the VV scattering. So, in this sense, the VV scattering process and the $pp \to VH^* \to VVV$ process are complementary to each other.

After determining the spin of the resonance, one can confirm the discovery of a heavy Higgs boson.

(vii) We also show the possibility of measuring the values of the anomalous coupling constants f_W and f_{WW} experimentally by measuring both the cross section and the $p_T(\text{leptons})$ distribution, the $p_T(J_1)$ distribution, the $\Delta R(\ell^+, J_2)$ distribution, and the $\Delta R(J_1, J_2)$ distribution (cf. Figs. 19 and 20). This will be a new measurement of the property of the nature at high energies, and will serve as a new high energy criterion for the correct new physics model. All new physics models predicting f_W and f_{WW} that are not consistent with the measured values should be ruled out. The necessary condition for surviving new physics models is that their predicted f_W and f_{WW} should be consistent with the measured values.

In weak-boson scattering, we imposed the forward-jet cut $p_T(j^f) > 35$ GeV to avoid the pileup events, while we did not impose that in VH associated production. This is because the transverse momenta of all the final state particles are large; e.g., our simulation shows that $p_T(J_2) > 100$ GeV, $p_T(J_1) > 200$ GeV [cf. Fig. 19(b)], and $p_T(\text{leptons}) > 400$ GeV [cf. Eq. (50)].

In all our predictions, only the statistical error is considered. We leave the study of the systematic error related to the details of the detectors to the experimentalists. Moreover, with the study of the jet shape, it may further suppress the backgrounds [49,50].

In Ref. [51] the 1-loop level contribution $gg \to VH$ in the SM was studied, and they showed that, although it is

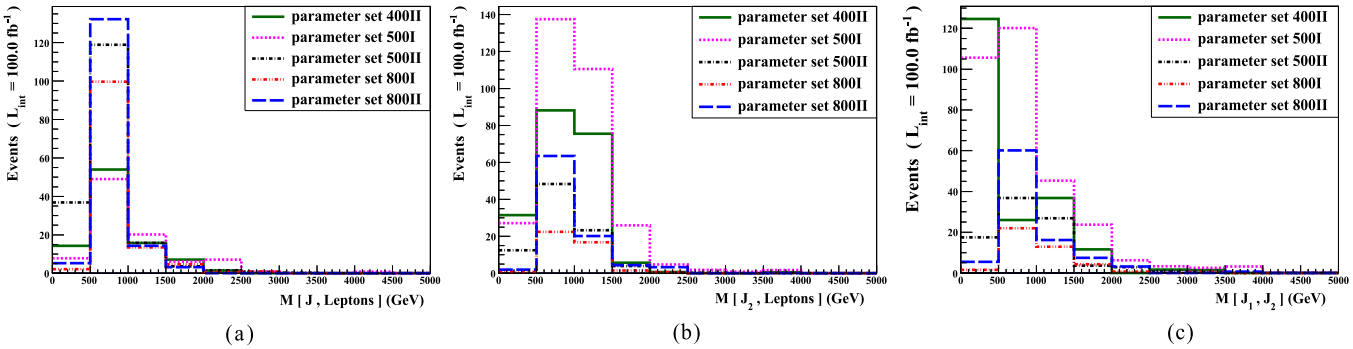

FIG. 21 (color online). Check of unitarity: (a) $M(J, \text{leptons})$ distribution in weak-boson scattering, (b) $M(J_2, \text{leptons})$ distribution, and (c) $M(J_1, J_2)$ distribution in the $pp \to VH^* \to VVV$ process.

smaller than the tree-level quark initiated contribution, this contribution can help to enhance the signal in VH associated production. This may also enhance the signal in our $pp \to VH^* \to VVV$ process. However, in our type-II examples, $C_t < 1$, so that the gluon initiated contribution is less important.

Finally, we make a check of the unitarity of our calculation. We know that the values of the anomalous couplings f_W and f_{WW}, which we take in this paper, are consistent with the unitarity constraints (Fig. 2). However, the unitarity constraints are obtained in the effective W approximation. Here we make a more realistic check based on our full simulation. In Fig. 21, we plot three invariant mass distributions up to a few TeV at the LHC in the VV scattering and the $pp \to VH^* \to VVV$ processes. We see that, in the high energy region, all distributions are monotonically decreasing to zero. This shows that there is no unitarity violation, so that our calculation is consistent with the unitarity requirement.

ACKNOWLEDGMENTS

We are grateful to Xin Chen for valuable discussions. We would also like to thank Tsinghua National Laboratory for Information Science and Technology for providing their computing facility. This work is supported by the National Natural Science Foundation of China under Grants No. 11135003 and No. 11275102.

[1] G. Aad *et al.* (ATLAS Collaboration), Phys. Lett. B **716**, 1 (2012); S. Chatrchyan *et al.* (CMS Collaboration), Phys. Lett. B **716**, 30 (2012).

[2] S. Chatrchyan *et al.* (CMS Collaboration), J. High Energy Phys. 06 (2013) 81; S. M. Consonni *et al.* (ATLAS Collaboration), arXiv:1305.3315.

[3] For instance, the International Linear Collider, the Future Circular Collider proposed at CERN, and the Circular Electron-Positron Collider proposed in China.

[4] R. Dashen and H. Neuberger, Phys. Rev. Lett. **50**, 1897 (1983).

[5] L. Susskind, Phys. Rev. D **20**, 2619 (1979).

[6] A. A. Savin *et al.* (CMS Collaboration), EPJ Web Conf. **28**, 09004 (2012).

[7] S. M. Consonni *et al.* (ATLAS Collaboration), arXiv:1305.3315.

[8] G. Aad *et al.* (ATLAS Collaboration), Phys. Rev. D **89**, 032002 (2014).

[9] There have been papers studying the constraints on the anomalous couplings of the discovered Higgs boson from the existing LHC data, leading to the conclusions that the anomalous couplings of this Higgs boson are consistent with zero at 95% C. L., and more data are needed. For example, T. Corbett, O. J. P. Eboli, J. Gonzalez-Fraile, and M. C. Gonzalez-Garcia, Phys. Rev. D **87**, 015022 (2013); **86**, 075013 (2012); C. Englert, A. Freitas, M. M. Mühlleitner, T. Plehn, M. Rauch, M. Spira, and K. Walz, J. Phys. G **41**, 113001 (2014).

[10] S. Chatrchyan *et al.* (CMS Collaboration), Report No. CMS-PAS-HIG-13-002 (unpublished).

[11] S. Chatrchyan *et al.* (CMS Collaboration), Report No. CMS-PAS-HIG-12-024 (unpublished).

[12] S. Chatrchyan *et al.* (CMS Collaboration), Report No. CMS-PAS-HIG-13-014 (unpublished).

[13] S. Chatrchyan *et al.* (CMS Collaboration), J. High Energy Phys. 01 (2014) 096.

[14] S. Chatrchyan *et al.* (CMS Collaboration), Report No. CMS-PAS-HIG-13-008 (unpublished).

[15] K. Hagiwara, S. Ishihara, R. Szalapski, and D. Zeppenfeld, Phys. Rev. D **48**, 2182 (1993).

[16] Let us consider if higher dimension operators can be introduced. We first look at the dim-5 operator $\bar{\psi}_f \gamma^\mu D_\mu H \psi_f = \bar{\psi}_f \gamma^\mu \partial_\mu H \psi_f + \cdots$. We can write it as $\partial_\mu(\bar{\psi}_f \gamma^\mu H \psi_f) - (\partial_\mu \bar{\psi}_f) H \psi_f - \bar{\psi}_f \gamma^\mu \partial_\mu \psi_f$. The first term (total derivative) contributes only on the surface at infinity, so that can be dropped. For the second and third terms, the Dirac equation $(\gamma^\mu \partial_\mu - m)\psi_f = 0$ reduces them to $m\bar{\psi}_f H \psi_f$ which is just the Yukawa form. So the dim-5 operator is actually equivalent to the dim-4 operator for on-shell fermions. It has been argued that the dim-6 operators also do not lead to new forms [17], as we are not interested in the multi-Higgs-fermion couplings which are irrelevant to our study. This is why we only take the Yukawa form here.

[17] J. A. Aguilar-Saavedra, Nucl. Phys. **B821**, 215 (2009).

[18] W. Buchmüller and D. Wyler, Nucl. Phys. **B268**, 621 (1986); C. J. C. Burges and H. J. Schnitzer, Nucl. Phys. **B228**, 464 (1983); C. N. Leung, S. T. Love, and S. Rao, Z. Phys. C **31**, 433 (1986).

[19] For a review, see M. C. Gonzalez-Garcia, Int. J. Mod. Phys. A **14**, 3121 (1999).

[20] B. Zhang, Y.-P. Kuang, H.-J. He, and C. P. Yuan, Phys. Rev. D **67**, 114024 (2003).

[21] V. Barger, T. Han, P. Langacker, B. McElrath, and P. M. Zerwas, Phys. Rev. D **67**, 115001 (2003).

[22] For example, G. Aad *et al.* (ATLAS Collaboration), Eur. Phys. J. C **72**, 2173 (2012); S. Chatrchyan *et al.* (CMS Collaboration), Eur. Phys. J. C **73**, 2610 (2013).

[23] G. J. Gounaris, J. Layssac, and F. M. Renard, Phys. Lett. B **332**,146 (1994); G. J. Gounaris, J. Layssac, J. E. Paschalis, and F. M. Renard, Z. Phys. C **66**, 619 (1995).

[24] M. Jacob and G . C. Wick, Ann. Phys. (N.Y.) **7**, 404 (1959).

[25] See, e.g., Refs. [10] and [11]. The CMS exclusion bounds in other Higgs decay channels are all weaker. See, e.g., Refs. [12], [13], and [14].

[26] N. D. Christensen and C. Duhr, Comput. Phys. Commun. **180**, 1614 (2009).
[27] J. Alwall, M. Herquet, F. Maltoni, O. Mattelaer, and T. Stelzer, J. High Energy Phys. 06 (2011) 128.
[28] G. Aad *et al.* (ATLAS Collaboration), Phys. Rev. Lett. **108**, 111803 (2012).
[29] S. Chatrchyan *et al.* (CMS Collaboration), Report No. CMS-PAS-HIG-13-001 (unpublished).
[30] G. Aad *et al.* (ATLAS Collaboration), Phys. Lett. B **732**, 8 (2014).
[31] S. Chatrchyan *et al.* (CMS Collaboration), Phys. Lett. B **726**, 587 (2013).
[32] J. de Favereau, C. Delaere, P. Demin, A. Giammanco, V. Lemaître, A. Mertens, and M. Selvaggi, J. High Energy Phys. 02 (2014) 057.
[33] Y.-H. Qi, Y.-P. Kuang, B.-J. Liu, and B. Zhang, Phys. Rev. D **79**, 055010 (2009).
[34] D. Stump, J. Huston, J. Pumplin, W.-K. Tung, H.-L. Lai, S. Kuhlmann, and J. F. Owens, J. High Energy Phys. 10 (2003) 046.
[35] T. Sjöstrand, S. Mrenna, and P. Skands, J. High Energy Phys. 05 (2006) 026.
[36] M. Cacciari, G. P. Salam, and G. Soyez, J. High Energy Phys. 04 (2008) 063.
[37] S. Chatrchyan *et al.* (CMS Collaboration), JINST **6**, P11002 (2011).
[38] J. Beringer *et al.* (Particle Data group), Phys. Rev. D **86**, 010001 (2012).
[39] J. Bagger, V. Barger, K. Cheung, J. Gunion, T. Han, G. A. Ladinsky, R. Rosenfeld, and C. P. Yuan, Phys. Rev. D **49**, 1246 (1994); **52**, 3878 (1995).
[40] J. M. Butterworth, B. E. Cox, and J. R. Forshaw, Phys. Rev. D **65**, 096014 (2002).
[41] Recently the CMS Collaboration made an analysis of identifying the fat jet from boosted W boson decay at the 8 TeV LHC (cf. Ref. [42]) showing that the uncertainty is less than 10%. The situation may be further improved in the 14 TeV run.
[42] S. Chatrchyan *et al.* (CMS Collaboration), arXiv:1410.4227v1.
[43] M. L. Mangano, M. Moretti, and R. Pittau, Nucl. Phys. **B632**, 343 (2002).
[44] J. Alwall *et al.*, Eur. Phys. J. C **53**, 473 (2008).
[45] S. Chatrchyan *et al.* (CMS Collaboration), Report No. CMS-PAS-HIG-13-008, 2013.
[46] S. Chatrchyan *et al.* (CMS Collaboration), Report No. CMS PAS TOP-11-009.
[47] D. J. Miller, S. Y. Choi, B. Eberle, M. M. Mühlleitner, and P. M. Zerwas, Phys. Lett. B **505**, 149 (2001).
[48] M. R. Buckley, H. Murayama, W. Klemm, and V. Rentala, Phys. Rev. D **78**, 014028 (2008).
[49] J. M. Butterworth, A. R. Davison, M. Rubin, and G. P. Salam, Phys. Rev. Lett. **100**, 242001 (2008).
[50] T. Han, D. Krohm, L.-T. Wang, and W. Zhu, J. High Energy Phys. 03 (2010) 082.
[51] C. Englert, M. MaCullough, and M. Spannowsky, Phys. Rev. D **89**, 013013 (2014).